International Journal of Applied Earth Observations and Geoinformation 116 (2023) 103153

Contents lists available at ScienceDirect

International Journal of Applied Earth Observation and Geoinformation

journal homepage: www.elsevier.com/locate/jag

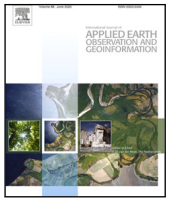

Multi-source knowledge graph reasoning for ocean oil spill detection from satellite SAR images

Xiaojian Liu [a], Yongjun Zhang [a,*], Huimin Zou [b], Fei Wang [a], Xin Cheng [a], Wenpin Wu [a], Xinyi Liu [a], Yansheng Li [a,c,**]

[a] School of Remote Sensing and Information Engineering, Wuhan University, Wuhan, 430079, China
[b] College of Global Change and Earth System Science, Beijing Normal University, Beijing, 100875, China
[c] Hubei Luojia Laboratory, Wuhan University, Wuhan, 430079, China

ARTICLE INFO

Keywords:
Multi-source knowledge graph
SAR image oil spill detection
Knowledge graph reasoning

ABSTRACT

Marine oil spills can cause severe damage to the marine environment and biological resources. Using satellite remote sensing technology is one of the best ways to monitor the sea surface in near real-time to obtain oil spill information. The existing methods in the literature either use deep convolutional neural networks in synthetic aperture radar (SAR) images to directly identify oil spills or use traditional methods based on artificial features sequentially to distinguish oil spills from sea surface. However, both approaches currently only use image information and ignore some valuable auxiliary information, such as marine weather conditions, distances from oil spill candidates to oil spill sources, etc. In this study, we proposed a novel method to help detect marine oil spills by constructing a multi-source knowledge graph, which was the first one specifically designed for oil spill detection in the remote sensing field. Our method can rationally organize and utilize various oil spill-related information obtained from multiple data sources, such as remote sensing images, vectors, texts, and atmosphere-ocean model data, which can be stored in a graph database for user-friendly query and management. In order to identify oil spills more effectively, we also proposed 13 new dark spot features and then used a feature selection technique to create a feature subset that was favorable to oil spill detection. Furthermore, we proposed a knowledge graph-based oil spill reasoning method that combines rule inference and graph neural network technology, which pre-inferred and eliminated most non-oil spills using statistical rules to alleviate the problem of imbalanced data categories (oil slick and non-oil slick). Entity recognition is ultimately performed on the remaining oil spill candidates using a graph neural network algorithm. To verify the effectiveness of our knowledge graph approach, we collected 35 large SAR images to construct a new dataset, for which the training set contained 110 oil slicks and 66264 non-oil slicks from 18 SAR images, the validation set contained 35 oil slicks and 69005 non-oil slicks from 10 SAR images, and the testing set contained 36 oil slicks and 36281 non-oil slicks from the remaining 7 SAR images. The results showed that some traditional oil spill detection methods and deep learning models failed when the dataset suffered a severe imbalance, while our proposed method identified oil spills with a sensitivity of 0.8428, specificity of 0.9985, and precision of 0.2781 under those same conditions. The knowledge graph method we proposed using multi-source data can not only help solve the problem of information island in oil spill detection, but serve as a guide for construction of remote sensing knowledge graphs in many other applications as well. The dataset gathered has been made freely available online (https://pan.baidu.com/s/1DDaqIljhjSMEUHyaATDIYA?pwd=qmt6).

1. Introduction

More and more scientific evidence shows that human society's activities have caused many environmental problems, wreaking havoc on Earth's ecosystems (Zhou et al., 2017). As one of the most harmful environmental problems, marine oil spills have attracted the attention of environmental protection departments and governments of various countries (de Moura et al., 2022). With the continuous growth of world oil consumption and transportation, they are occurring more

* Corresponding author.
** Corresponding author at: School of Remote Sensing and Information Engineering, Wuhan University, Wuhan, 430079, China.
E-mail addresses: liuxiaojian2018@whu.edu.cn (X. Liu), zhangyj@whu.edu.cn (Y. Zhang), hmzou@mail.bnu.edu.cn (H. Zou), flyking@whu.edu.cn (F. Wang), chengxin_w@whu.edu.cn (X. Cheng), ones_w@whu.edu.cn (W. Wu), liuxy0319@whu.edu.cn (X. Liu), yansheng.li@whu.edu.cn (Y. Li).

https://doi.org/10.1016/j.jag.2022.103153
Received 2 August 2022; Received in revised form 10 December 2022; Accepted 10 December 2022
Available online 14 December 2022

frequently. Oil spills into the ocean can result in a severe lack of oxygen on the ocean surface and the death of a great number of fish, shrimp, and marine birds. When the oil slick is swept up on the beach by the waves, it will adhere to the sand, harming mariculture and coastal tourism sites. Timely, accurate, and comprehensive monitoring of the sea surface will help reduce the occurrence of this pollution.

Among the many available oil spill monitoring tools, Synthetic Aperture Radar (SAR) satellite is one of the most powerful since it can monitor marine oil spills continuously and in all weather conditions (Marghany et al., 2009). It is unmatched by any other surveillance tool. Spilled oil reduces the roughness of the ocean surface, causing the Bragg waves to decay. This change typically presents as dark spots on SAR remote sensing images. However, some atmospheric and oceanic phenomena, such as low winds, upwelling, and abnormal chlorophyll-a concentration, also increase the smoothness of the ocean surface and show dark spots (named "lookalikes") on SAR images (Guo and Zhang, 2014). These lookalikes account for the great majority of dark spots, posing a significant barrier to oil spill detection.

Generally, there are two kinds of approaches to detect oil spills on the ocean surface. The first kind consists of deep learning methods, and the second is the traditional methods based on artificial features. The traditional oil spill detection methods usually consist of three stages: dark spot segmentation, feature extraction, and dark spot classification (Mera et al., 2017). Dark spot segmentation is the basic step, and its purpose is to perform high-precision segmentation of all the dark spots on SAR images. A variety of fast or high-performance dark spot segmentation algorithms have been developed over time, including recurrent neural network (Topouzelis et al., 2006), Otsu threshold + post-processing (Chehresa et al., 2016), an intelligent hybrid detection system that integrates semi-automatic and automatic procedures (Genovez et al., 2017), and Segnet (Guo et al., 2018). The feature extraction process must first locate features for distinguishing oil spills from lookalikes. A variety of types and quantities of features suitable for oil spill detection were found in the literature. Solberg et al. (1999) extracted 11 features; Keramitsoglou et al. (2006) used 14 features; Topouzelis et al. (2009) summarized the 25 most commonly used features; Chehresa et al. (2016) used 74 features; and Mera et al. (2017) used 52 features. Although the number of features may vary, they can generally be classified into four categories: geometric features, physical features, texture features, and context features. After feature extraction, a suitable classifier then must be chosen to distinguish between oil spills and lookalikes. Many classifiers have been proven to achieve excellent classification results on some given datasets, such as multi-layer perceptron (MLP) (Topouzelis et al., 2007), decision tree (Vyas et al., 2015), Bayesian network with Naïve Bayes structure (Chehresa et al., 2016), and support vector machine (SVM) (Mera et al., 2017). However, challenges still exist. On the whole, these conventional techniques focus more on excavating and utilizing image information to identify oil contamination. They ignore the power of semantic relationships between dark spots and other entity objects, resulting in the problem of information islands.

Different from traditional oil spill detection methods, deep learning methods can directly identify oil spills from SAR images. In recent years, they have experienced rapid development due to improvements in SAR sensors. Yu et al. (2018) developed an oil spill detection method via adversarial f-divergence learning, using the f-divergence to measure the probabilistic difference between the ground truth and the generated oil spill segmentation and then minimizing the f-divergence to detect oil spills. Krestenitis et al. (2019) compared five classic neural networks classifiers and found that the DeepLabv3+ model performed the best on their dataset. Li et al. (2021b) proposed a multi-scale conditional adversarial network for oil spill detection that can be used in limited-sample situations. Fan et al. (2021) introduced a feature merged network, using the original SAR images and high-frequency feature information extracted by threshold segmentation as the input of the semantic segmentation network to improve the performance of oil spill detection. Compared with traditional methods, deep learning technologies are more intelligent. They can automatically identify oil spills based on the information in the image, which includes various entity objects and semantic relationships. However, they still only take remote sensing images as the information source. Although some entity objects such as ships, sea ice, coastlines, etc., can also be identified from the image to help identify oil spills, as a whole, the amount of information available is still limited. More auxiliary information about the oil spill, such as oil pipelines, ship trajectories, and so on, needs to be considered, which is usually difficult to obtain from remote sensing images. Furthermore, problems such as lack of a semantic connection between information, imbalanced training sets, and hard-to-find knowledge, continue to be challenges for detecting oil spills (Topouzelis, 2008).

To improve the performance of oil spill detection methods, more auxiliary information must be used, such as chlorophyll-a distribution, sea temperature difference, rainfall distribution, distances from dark spots to the ship's trajectory, etc (Alpers et al., 2017). The recent development of the knowledge graph is having enormous implications for a wide variety of processes. Knowledge graphs use entities to represent real-world things and relationships to denote the connections between them. This unified knowledge description framework is very conducive to sharing and utilizing knowledge. Some researchers believe that the coupling of knowledge models and deep learning technology is an effective means to solve complex scene modeling (Reichstein et al., 2019). Until now, knowledge graph technology has been implemented in various industries, such as geoscience, medicine, and so on. It is closely related to natural language processing (NLP). However, remote sensing knowledge graph research is still in its infancy (Hao et al., 2021). To facilitate the organization and management of data, Hao et al. (2021) extracted concepts in the surveying and remote sensing domain to construct a knowledge graph with 1024 nodes and 1295 relations. Li et al. (2021a) constructed a remote sensing scene knowledge graph containing 117 entities and 26 relationships and then combined it with deep learning techniques to propose a method for zero-shot remote sensing image scene classification. Recently, Li et al. (2022) combined knowledge graph ontology reasoning with deep learning techniques in a collaborative boosting framework that can improve the performance of remote sensing image semantic segmentation. Nevertheless, the scale of existing remote sensing knowledge graphs is limited, and the applications are relatively simple. Furthermore, their data sources remain relatively single, consisting mainly of structured tables, unstructured texts, and semi-structured data between structured and unstructured data. Other types of data, such as remote sensing images, vector data, and application model data, are underutilized (Hao et al., 2021), and there is a relative lack of effective techniques for extracting knowledge from them (Ge et al., 2022), resulting in significant information loss. To the best of our knowledge, no one has yet used knowledge graph technology to identify oil spills on the sea surface.

To meet the above challenges and provide a reference for the construction of remote sensing knowledge graphs in the future, this study explores for the first time using multi-source data, such as remote sensing images, atmospheric and ocean model data, vector data, and text, to build a knowledge graph for oil spill detection. Our knowledge extraction techniques were no longer limited to NLP, but included some remote sensing image processing techniques. Data sources for oil spill detection were not limited to satellite remote sensing images. Some oil spill-related information had been linked together by rational organizations and no longer existed in isolation. With 172,684 entities, 9,873,312 relationships, and 274 attributes, our knowledge graph was significantly larger in scale than existing remote sensing-type knowledge graphs. All of the abbreviations used in this study were listed in Table 1. The main contributions of this study are given as follows:

(1) We proposed a novel multi-source knowledge graph construction method for oil spill detection. Expert knowledge was used to design the semantic types and semantic relationships of the oil

Table 1
Abbreviations used in this article.

No.	Abbreviations	Descriptions	No.	Abbreviations	Descriptions
1	AIS	Automatic Identification System	19	MERIS	Medium Resolution Imaging Spectrometer
2	ASAR	Advanced Synthetic Aperture Radar	20	MLP	Multi-layer perceptron
3	BASS	Bayesian Adaptive Superpixel Segmentation	21	MODIS	Moderate-resolution Imaging Spectroradiometer
4	CMOD5	C-band model 5	22	NLP	Natural Language Processing
5	DeeperGCN	Deeper Graph Convolutional Neural Network	23	RDF	Resource Description Framework
6	ECMWF	European Centre for Medium-Range Weather Forecasts	24	SAR	Synthetic Aperture Radar
7	ENVISAT	Environmental Satellite	25	SeaWiFS	Sea-viewing Wide Field-of-view Sensor
8	ESA	European Space Agency	26	SDGCN	Superpixel-based Deeper Graph Convolutional neural Network
9	FN	False Negative	27	SNAP	Sentinel Application Platform
10	FP	False Positives	28	SVM	Support Vector Machine
11	GAC	Global Area Coverage	29	SVM-RFE	Support Vector Machines Recursive Feature Elimination
12	GCN	Graph Convolutional Neural Network	30	TN	True Negative
13	GNN	Graph Neural Network	31	TP	True Positives
14	HELCOM	Helsinki Commission	32	UNet	Unity Networking
15	HH	Horizontal Transmit, Horizontal Receive (antenna polarization)	33	VIIRS	Visible Infrared Imaging Radiometer Suite
16	HYCOM	HYbrid coordinate ocean model	34	VV	Vertical Transmit, Vertical Receive (antenna polarization)
17	LAC	Local Area Coverage	35	WSM	Wide Swath Mode
18	MCAN	Multiscale Conditional Adversarial Network			

spill detection knowledge graph to guide its construction. All the vectors, remote sensing images, and objects segmented from SAR images were treated as identities; and the features extracted from the remote sensing images and atmospheric ocean model data were stored as dark spot entity attributes, with the vector attributes directly taken as entity attributes.

(2) Thirteen new features for oil spill detection were extracted to improve oil spill detection performance.

(3) An oil spill reasoning method was designed based on rule reasoning and a graph neural network algorithm, which mitigated the impact of imbalanced classes in a dataset.

(4) We made public all of the data utilized in this research, including 35 SAR images with detected oil spills and some processed auxiliary data such as vector data, optical remote sensing image products, atmospheric and ocean model data, and so on.

2. Study region and dataset

In this section, we selected the Baltic Sea as our study area, where oil spills occurred frequently, and then provided a detailed introduction to the datasets we used.

2.1. Area of interest

The European Baltic Sea is a crucial waterway in Northern Europe. It surrounds the landing ground on all sides and is located between the nine countries of Sweden, Russia, Denmark, Germany, Poland, Finland, Estonia, Latvia, and Lithuania. With the development of industry and shipping, the Baltic Sea has become strategically important. At the same time, the Baltic Sea's marine environment and coastline ecology are continually threatened by oil spills. During the period 1998–2017, 4525 oil spills were observed during aerial surveillance flights by the Baltic Marine Environment Protection Commission – HELCOM Contracting Parties. According to Konik and Bradtke (2016), there were few oil rigs in the Baltic Sea, and the crude oil demand of countries around the Baltic Sea must be met primarily through imports. Additionally, HELCOM did not provide some relevant reports on natural seepages. Illegal oil discharges are most common in the central Baltic Sea and along shipping routes and pipelines, as shown in Fig. 1. A large quantity of oil pollution has caused severe economic losses to the Baltic Sea and is destroying the living environment of marine organisms. Taking this marine area as the research area, we constructed a novel knowledge graph for monitoring marine oil spills.

2.2. Dataset

To construct our knowledge graph for oil spill detection, we collected, in accordance with the oil spill information released by HELCOM from 2006 to 2011, 35 ASAR products with WSM in VV polarization from the ENVISAT satellite as a main information source. ENVISAT ASAR was developed by ESA and operated in a variety of modes in the C band. As shown in Table 2, the WSM we used was a superior instrument for oil slicks on the ocean's surface, providing an excellent mix of radiometric quality and wide coverage. It had a swath width of 405 km, a resolution of 150 m, and an incidence angle range of 15 to 45 degrees, making it ideal for detecting large-scale oil spills. This mode provided two types of polarization: VV polarization and HH polarization. According to Solberg (2012), VV polarization can generate more backscatter from the ocean surface than HH polarization and is frequently used in the detection of oil spills (Mera et al., 2017). We only used VV polarization in this study. Fig. 2 shows the acquisition date distribution for the ASAR products we used. As can be seen, more than half of the images were collected between 2007 and 2008, with 2009 and 2011 having the lowest proportion. Furthermore, 85% of the images were captured between April and October, with only a few captured during the winter. Before being used, SAR images must undergo preprocessing, which typically includes radiometric calibration, reprojection, and speckle filtering. These steps were carried out using SNAP (Misra and Balaji, 2017), which is a common architecture for ESA Toolboxes. The goal of radiometric calibration is to capture pixels that accurately represent the reflecting surface radar backscatter. After that, the calibrated images are then reprojected into a coordinate system that is close to the real world. For speckle filtering, a 3×3 Lee filter (Mansourpour et al., 2006) was chosen. The Lee filter has proved to be a very successful filter in the image processing of oil spill detection (Genovez et al., 2017). Following preprocessing, we used SDGCN (Liu et al., 2022) technique to detect dark spots. This method can smooth SAR image noise and improve the segmentation performance of some dark spots with weak borders and small regions (Liu et al., 2022). Ultimately, we acquired 181 oil spill patches and around 170,000 lookalikes from 35 SAR images, constructing a dataset that was extremely close to reality and challenging for spill identification. Fig. 3 shows several different oil spills detected by these SAR images. These oil spills vary in shape, size, and brightness due to the effects of advection (Guo and Wang, 2009), evaporation (Reed et al., 1999), emulsification (Xie et al., 2007), and the amount of leaking (Taravat et al., 2013), making them more difficult to identify.

According to Alpers et al. (2017), we also collected important auxiliary data, such as vector data, atmospheric ocean model data, and a small amount of text data, to help distinguish between the oil slicks and the lookalikes. Fig. 4 shows the various data we employed.

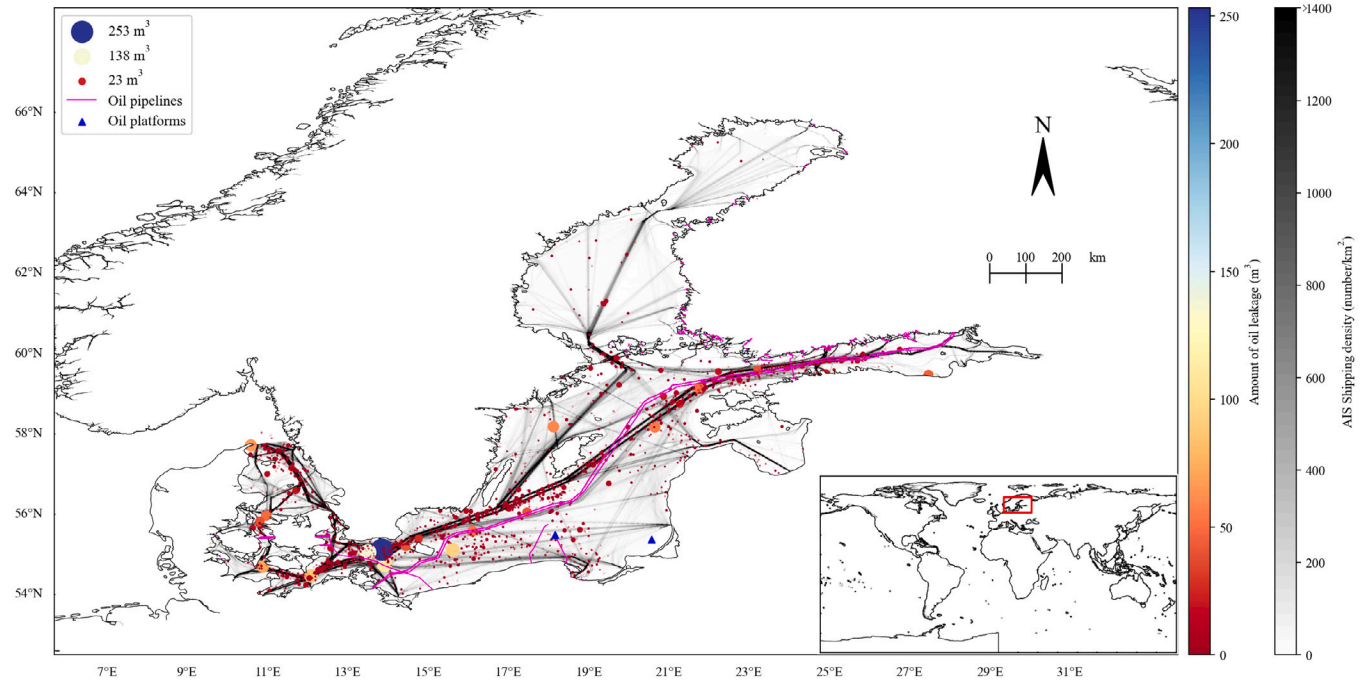

Fig. 1. Oil spills in the Baltic Sea between 1998 and 2017. The data comes from the HELCOM map and data service (http://maps.helcom.fi/website/mapservice/index.html). The amount of oil leakage is represented by the size and color of the dot. The blue triangles and magenta lines represent oil platforms and oil pipelines, respectively. Additionally, gray rendering indicates the annual average AIS shipping density from 2006 to 2011.

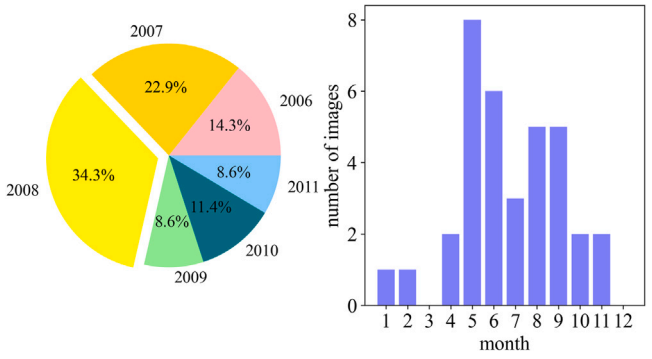

Fig. 2. The acquisition dates of SAR images. The left panel shows the proportion of SAR images acquired in various years, while the right panel displays the number of SAR images acquired in different months.

Furthermore, Table 3 depicts the details of these data, such as their source and resolution. The vector data, all provided by HELCOM, included the Baltic coastline, as well as 515 pipelines, 23 oil terminals, 2 oil platforms, 16 oil and gas refineries, 320 ports, and 7 sub-basins in this region. The wind speed data was acquired by inverting SAR images using the CMOD5 model (Hersbach et al., 2007) and had the same pixel size as the SAR image. Data on air-sea temperature differences, convective rainfall rates, and chlorophyll-a concentrations were provided by ECMWF. They all used a horizontal regular latitude–longitude grid that covered the whole globe. In the Baltic Sea, the former two have a resolution of around 27.8 km × 13.9 km, whereas the latter has a resolution of about 4.7 km × 2.3 km. The air-sea temperature difference and convective rainfall rate data were hourly data, whereas the chlorophyll-a concentration data consisted of daily composites of merged sensor (MODIS Aqua, MERIS, VIIRS, SeaWiFS LAC & GAC) products, which were only available over cloud-free and ice-free areas. The sea surface speed data were available from HYCOM which had a temporal frequency of 3 h. In the horizontal direction, it used a regular latitude–longitude grid, with a resolution of around 4.4 km × 4.4 km in

Table 2
Main characteristics of the The ASAR Wide Swath Mode.

Mode	Polarization	Resolution	Incidence	Swath
Wide Swath	VV	150 m	15–45°	405 km

the Baltic Sea region. Both the sandbank location data and the annual AIS shipping density data were raster data available from HELCOM, and their spatial resolutions were 1.6 km and 1 km, respectively. For consistency, the atmospheric and oceanic model data were converted into raster data format as well. Furthermore, the above data were all sampled at the same resolution as the SAR images using bilinear interpolation technology (Kirkland, 2010). This interpolation approach was fast and had specific effects, so it was the most popular among image researchers. Temporally, the air-sea temperature differential, convective rainfall rate, and sea surface speed data were interpolated by cubic interpolation to obtain the data at the same moment as the SAR. Since chlorophyll-a concentration data was only available when there was no ice or cloud cover, making temporal interpolation difficult, so we kept the data in a daily format.

3. Methods

The multi-source knowledge graph construction and knowledge reasoning methods for oil leak detection we proposed are introduced in this section, and Fig. 5 depicts the specific workflow. The subsections that follow go through the various core techniques we used, such as oil spill detection knowledge modeling, knowledge extraction from multi-source data, knowledge storage, oil spill detection based on knowledge graph reasoning, and specific experimental settings.

3.1. Oil spill detection knowledge modeling

Generally, there are four kinds of methods for building a knowledge system: (1) the expert method (Zheng et al., 2021), (2) the reference method (Yang et al., 2021), (3) the induction method (Hao et al., 2021), and (4) the hybrid method (Yu et al., 2017).

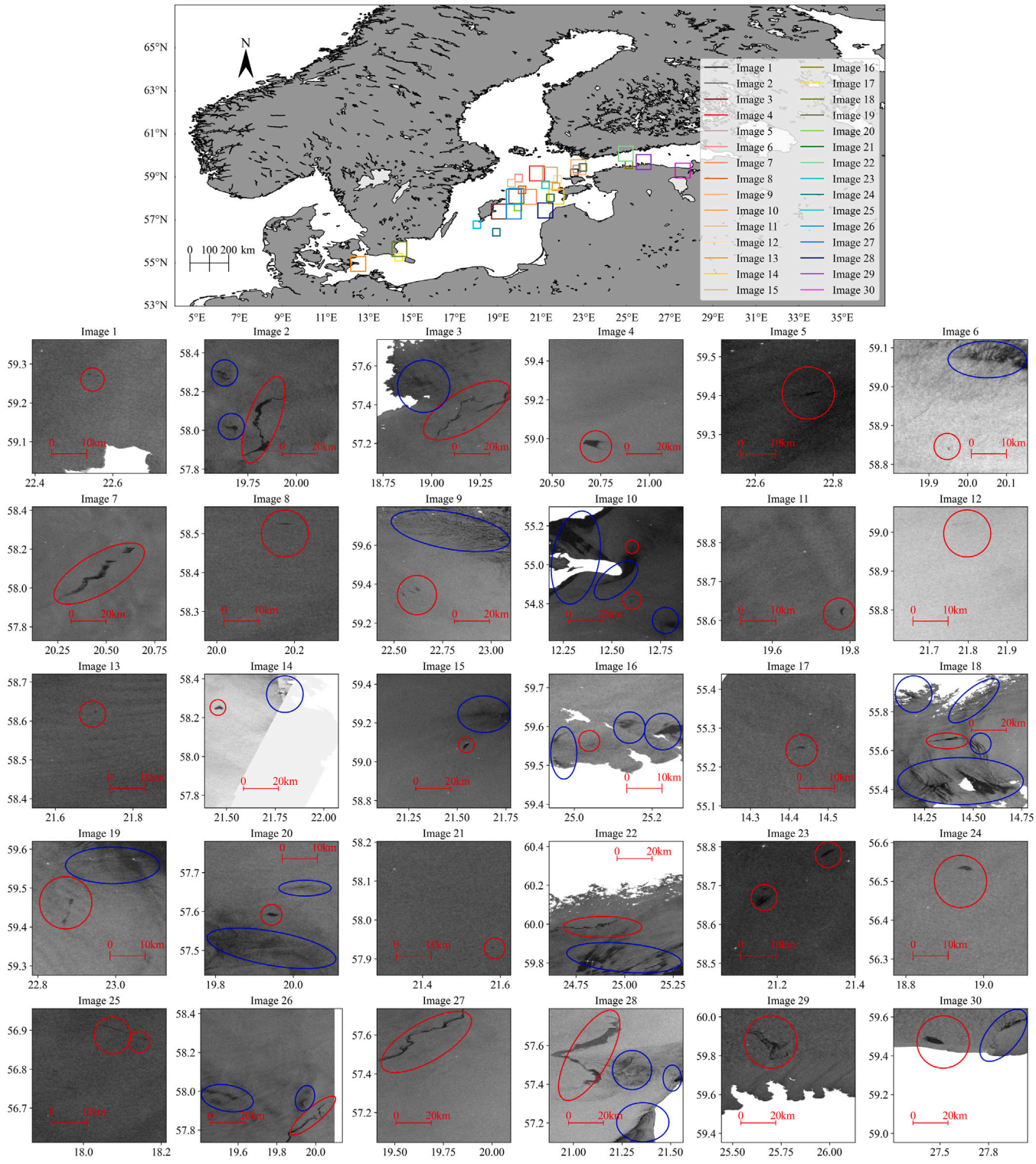

Fig. 3. Different examples of SAR oil spill images. The top panel shows the location of all SAR images. In these images, the dark spots located in the red area are oil spills, while the dark spots in the blue area are lookalikes. (For interpretation of the references to color in this figure legend, the reader is referred to the web version of this article.)

Since the purpose of our work was simple and clear, we adopted the expert method to design the semantic types and semantic relations of the knowledge graph. Fig. 6 shows the design results. The semantic types consist of two categories: entities and events. Entities are divided into conceptual entities and physical entities. Conceptual entities include dark spots segmented from SAR images, types of dark spots, the polarization mode of the SAR images, and the time of acquisition of the SAR images. Physical entities mainly refer to real world things, such as oil and gas refinery, oil platform, oil terminal, pipeline, sea, sea subbasin, satellite platform, and remote sensing imagery. Events comprise phenomena and activities with the differences between them being that the former refers to the appearance but not necessarily the participation of multiple parties, and the latter must be multiparty. Phenomena include platform oil spills, ship oil spills, biological oil spills, upwelling,

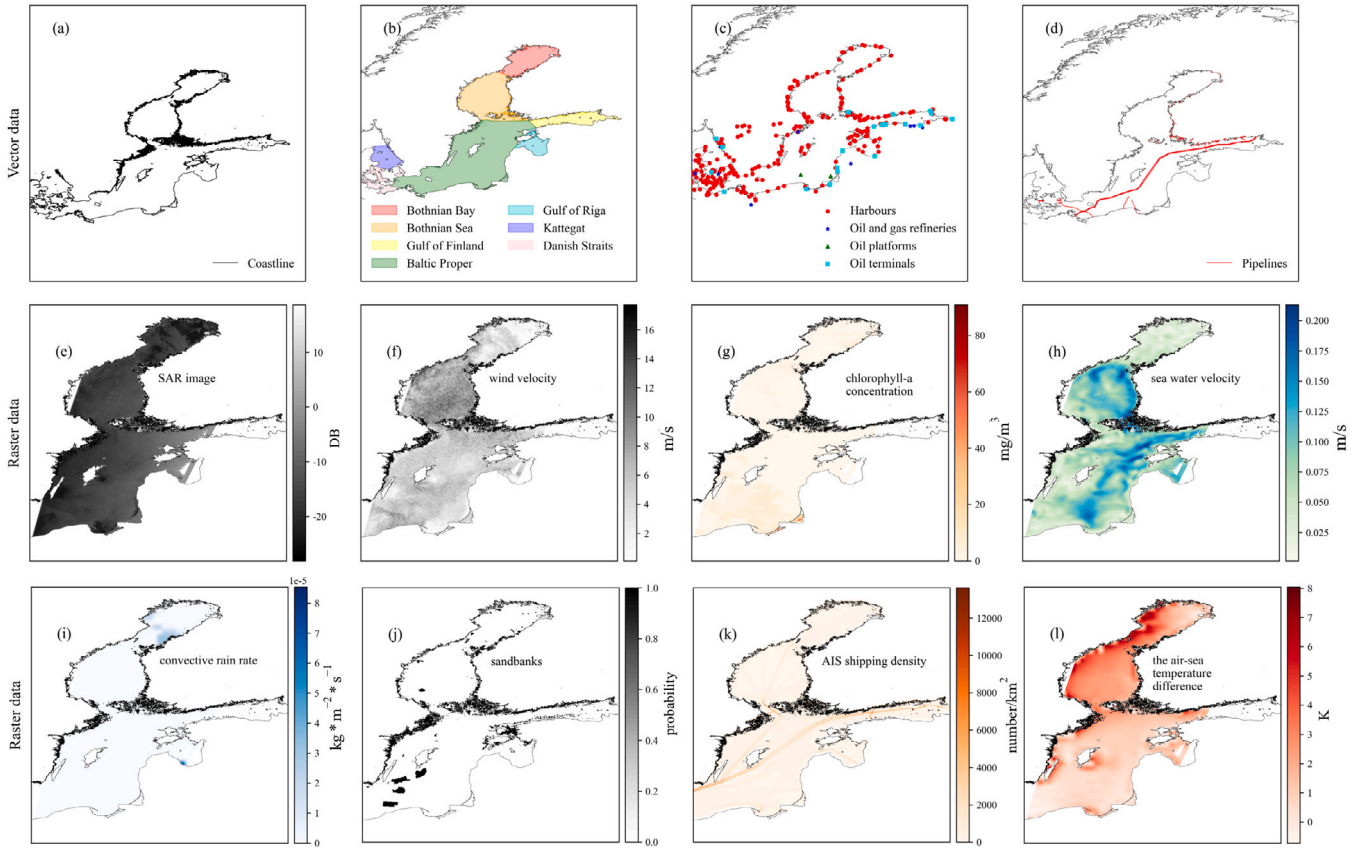

Fig. 4. Research data used to construct the knowledge graph. Panels a to d display vector data from the HELCOM Map and data service. Panel e shows an example of the ENVISAT ASAR imagery provided by ESA. Panel f exhibits wind speed inversion data derived using the CMOD5 geophysical model function. Panels g, i, and l respectively show chlorophyll-a concentration data, convective rainfall rate data, and air-sea temperature difference data, all from ECMWF. Panel h is ocean water velocity data from the HYCOM model. And panels j and k are derived from sandbank location data and AIS shipping density data provided by HELCOM.

Table 3
The primary data used in oil spill detection, as well as its type, source, time interval, and resolution.

Name	Type	Source	Time interval	Resolution (latitude–longitude grid)
coastline, pipeline, oil terminals, oil and gas refineries, ports, sub-basin	vector data	HELCOM	–	–
SAR image	raster data	ESA	–	150 m × 150 m
wind speed data	raster data	CMOD5	–	150 m × 150 m
sandbanks data	raster data	HELCOM	–	1.6 km × 1.6 km
AIS shipping density data	raster data	HELCOM	1 year	1 km × 1 km
chlorophyll-a concentration data	model data	ECMWF	1 day	2.3 km × 4.7 km
sea water velocity data	model data	HYCOM	3 h	4.4 km × 4.4 km
convective rain rate	model data	ECMWF	1 h	13.9 km × 27.9 km
air-sea temperature difference data	model data	ECMWF	1 h	13.9 km × 27.9 km

low wind speed, convective rain, and so on. Since our main focus is on the oil spill detection function of the knowledge graph, no detailed activities were designed. The semantic relations have five categories: (1) spatial relations, (2) time relations, (3) functional relations, (4) conceptual relations, and (5) physical relations. The spatial relations describe the positional relationship between dark spots and dark spots, dark spots and oil terminals, dark spots and pipelines, dark spots and ports, etc., and include intersects, *close to*, *is in*, and *is closest to*. The time relation describes the time sequence of satellite image capture and the order of events that occurred, which include *is before* and *was obtained in*. The functional relation mainly refers to the causal relationship, such as what event caused the dark spot phenomenon, and the physical relation is primarily the *contained* relationship, such as which basins are contained in the Baltic Sea. The conceptual relation is comprised of terms such as *come from*, *belong to*, *is*, and *is polarized by* (e.g., the country to which a port belongs, the image the oil pollution comes from, and the polarization mode of the SAR image). Although various semantic types and relations are constructed, not all of them are used in practice.

3.2. Knowledge extraction from multi-source data

The aim of our knowledge extraction process is to obtain knowledge from massive data utilizing the information extraction method. The subsections describe the knowledge extraction technique for our oil spill detection knowledge graph, including entity extraction, attribute extraction, and relation extraction.

3.2.1. Entity extraction

In the domain of remote sensing, the main data source is no longer text but rather vectors and raster images, which requires image processing technology to extract knowledge. In this study, vectors, including

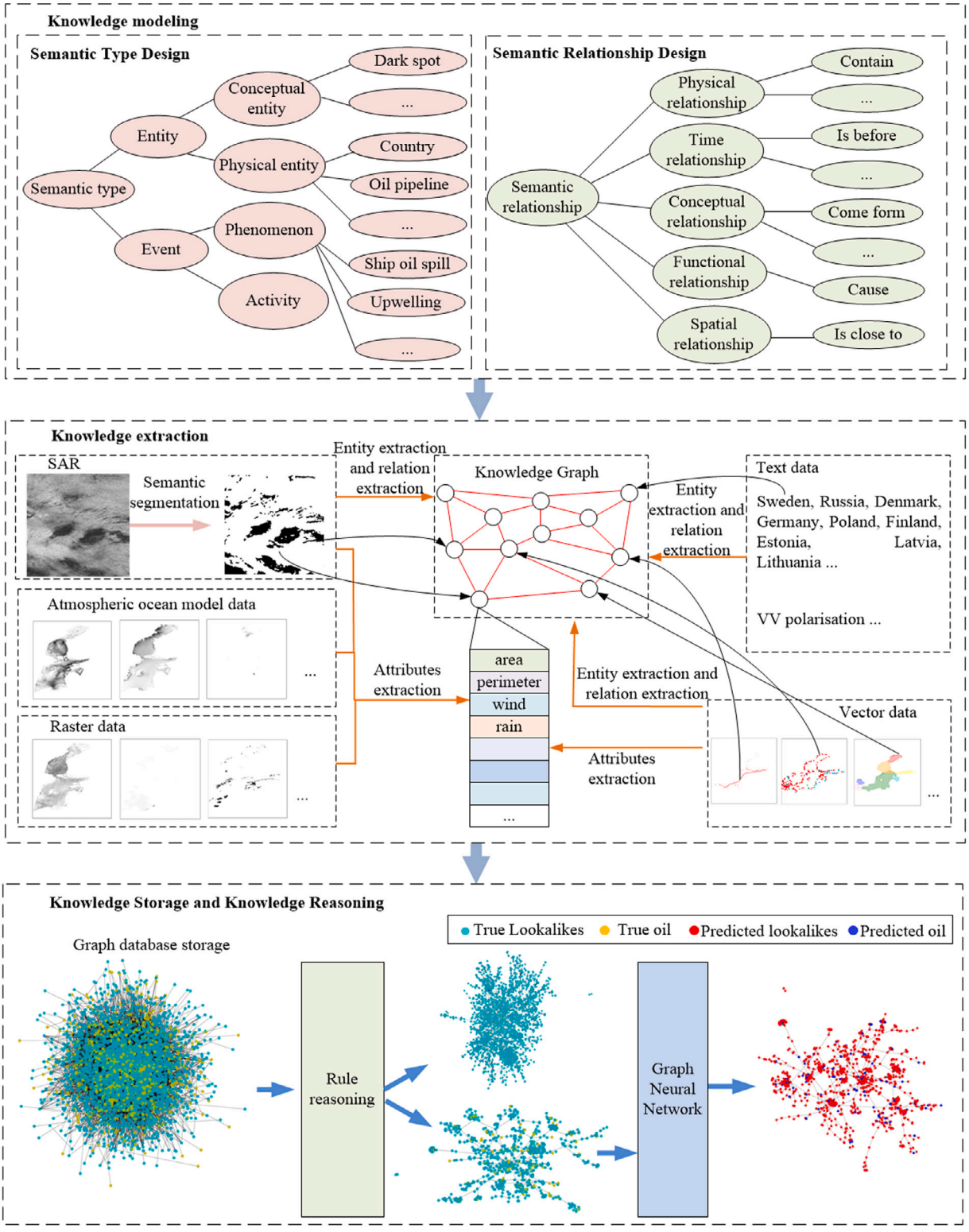

Fig. 5. The workflow of multi-source data-driven oil spill detection knowledge graph construction and application.

point features (oil terminals, harbors, oil and gas refineries, oil platforms), line features (pipelines), and polygon features (basins), could be directly used as separate entities without further processing. The objects detected from the images by the interpretation method could be taken as entities as well. Therefore, the segmented dark spots on SAR images were used as oil spill candidate entities, which were obtained using an intelligent segmentation method based on SDGCN (Liu et al., 2022). The algorithm thus converted the images into graphs and precisely extracted dark spots directly from the SAR images, and the remote sensing images with dark spots detected also were considered as

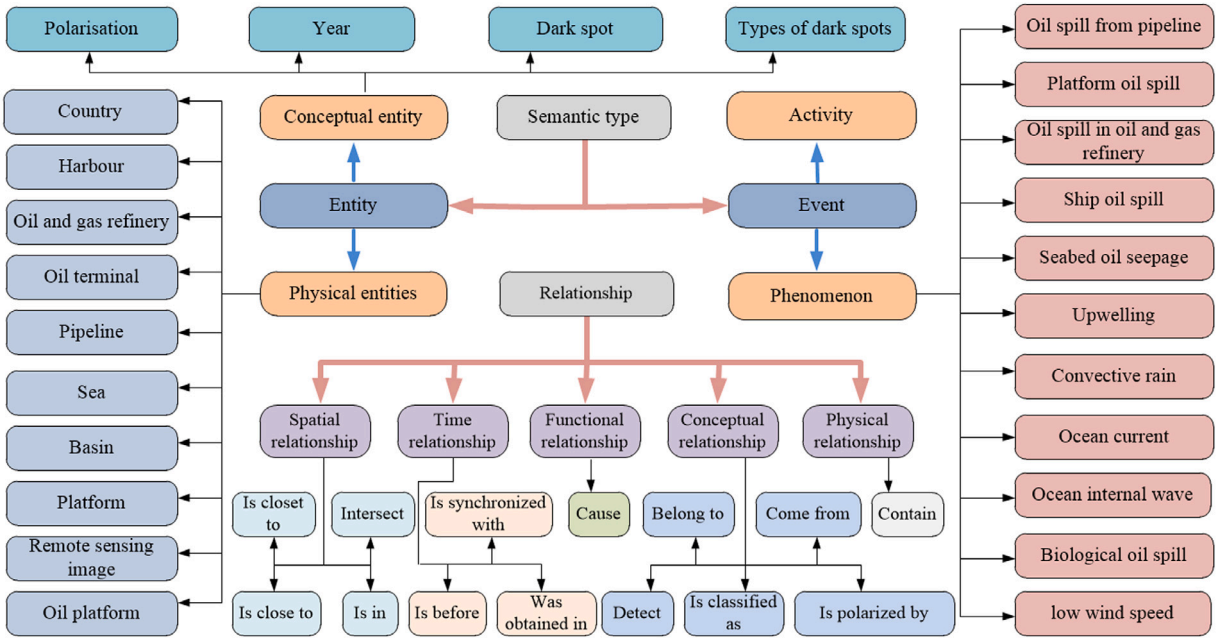

Fig. 6. Semantic type and semantic relationship.

entities. For convenience, the remaining few entities, such as country, time, ocean, and polarization, were manually extracted direct from the text data.

3.2.2. Attribute extraction

Attribute extraction is also an important component in knowledge extraction. Its goal is to collect the attribute information of specific entities from various data sources and can make the knowledge graph more complete. In this study, the attributes of vectors such as seaports, oil and gas refineries, oil terminals, oil platforms, pipelines, basins, etc.,can be directly extracted and used as entity attributes. The entities extracted from raster images, on the other hand, required additional feature calculations. Previous works in the literature have offered many kinds of features for oil spill detection. The 52 features (including 23 physical features, 27 geometrical features, and two textural features) used by Mera et al. (2017) were extracted and used as the dark spot entity attributes in this work. They were all acquired simultaneously with the SAR images. All of these features are itemized in our supplementary materials. In order to further enhance the identification of oil spills, we extracted 13 new features as supplements, including six physical features and seven contextual features, as shown in Table 4. Among them, DC, DP, DH, DOGR, DT, and DOR were obtained by calculating the distance between the dark spots on the SAR images and the actual external objects, so they were also acquired at the same time as the SAR images. Rm, Sm, and Tm were calculated from the convective rain rate data, seawater velocity data, and air-sea temperature difference data, respectively. These data had been interpolated to the same moment as the SAR image before being used. Sp was calculated using the dark spots on the SAR image and fixed sandbank position data. Both AISdm and DAIS were calculated using SAR images and annual AIS shipping density maps produced by HELCOM. By threshold segmentation, we obtained ship routes from the annual density maps. DAIS represented the distance between the dark spots on the SAR images and these ship routes, while AISdm represented the mean annual shipping density of these dark spot areas. Because optical sensors were limited by weather conditions, the chlorophyll-a concentration data we used consisted of daily composites of merged sensor products. Cam became the mean daily chlorophyll-a concentration of the dark spot areas on the SAR images as a result. Explanations for all the features we used can be found in our supplementary materials and in Mera et al. (2017).

3.2.3. Relation extraction

In a knowledge graph, relations are defined as the connections between two or more entities. Relation extraction identifies the given semantic relationships between entities. As shown in Fig. 7, the relations between entities in this study were extracted by referring to the designed semantic relations at the model layer. For dark spots and their source images, a directional relationship called *come from* was constructed between them. Then, the remote sensing images were linked together by establishing time-series relationships. At the same time, one relationship called *was obtained in* was built between the remote sensing images and the year. Further, the relations between the remote sensing image and the platform, as well as the remote sensing image and the polarization mode were established, called *come from* and *is polarized by*, respectively. Spatially, using a Python library (geographiclib) to calculate distances and find the oil and gas refineries, ports, oil terminals, pipelines, and oil platforms closest to dark spots, the relationships between them called *is closest to* were established. These distances then were stored as their attributes. In addition, when oil pipelines intersected dark spots, intersection relationships were established between them. Oil terminals, ports, and oil platforms comprised a relation called *belong to* with their countries, respectively. For dark spots and basins, relations called *is in* were established for them when some dark spots were in a given sea basin. Subsequently, the *contain* relations between the Baltic Sea and sea basins were extracted. The spatial relationship between dark spots on the same SAR image was established as follows: (1) the shortest distance between any two dark spots on the same image was calculated; (2) when the connecting line with the shortest distance between two dark spots did not cross other dark spots or land, a relationship named *is close to* was established between them; and (3) the shortest distance and direction were taken as attributes of this relation.

3.3. Oil spill detection based on knowledge graph reasoning

After the above work, a primary knowledge graph was established. As shown in Table 5, this knowledge graph includes 172,684 entities, 9,873,312 relationships, and 274 attributes. Among them, 171,731 entities were dark spots, and 234 attributes were dark spot attributes. Since the knowledge graph was too large, we visualized some nodes and relationships in a knowledge subgraph constructed using one SAR

Table 4
Seven contextual features and six physical features of dark spots proposed in this study.

No.	Feature	Code	Feature type	No.	Feature	Code	Feature type
1	Distance to coastline	DC	Contextual	8	Mean convective rain	Rm	Physical
2	Distance to pipeline	DP	Contextual	9	Sea speed mean	Sm	Physical
3	Distance to harbor	DH	Contextual	10	AIS shipping density mean	AISdm	Physical
4	Distance to oil and gas refinery	DOGR	Contextual	11	Chlorophyll-a concentration mean	Cam	Physical
5	Distance to AIS ship track	DAIS	Contextual	12	Mean of air-sea temperature difference	Tm	Physical
6	Distance to oil terminal	DT	Contextual	13	Proportion of area occupied by sandbanks	Sp	Physical
7	Distance to oil platform	DOP	Contextual				

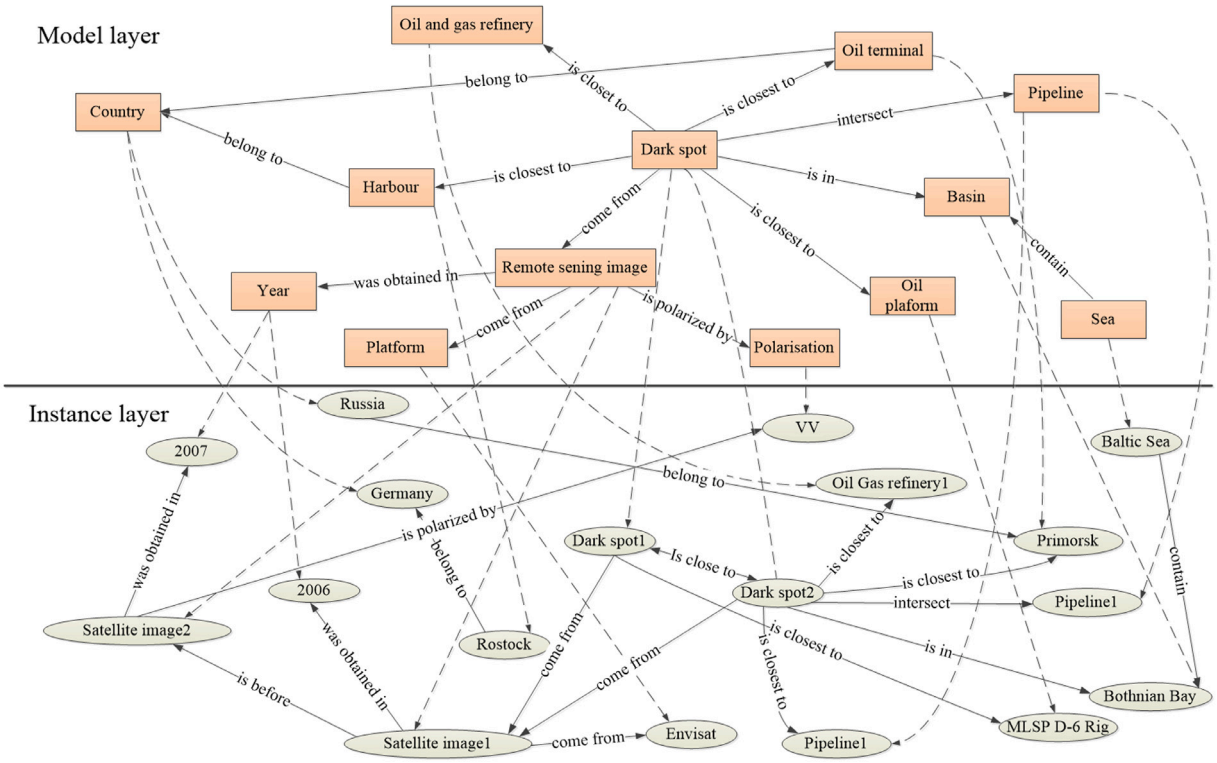

Fig. 7. The model layer and instance layer of the knowledge graph.

Table 5
Statistics of entities and relationships in the knowledge graph of oil spill detection.

Entity types	Entity numbers	Relations	Relation numbers
Seas	1	Belong_to	362
Year	6	Is_close_to	8680248
Remote_sensing_image	35	Come_from	161411
Polarization	4	Contain	7
Platforms	15	Intersect	2438
Pipelines	515	Is_before	34
Oil_terminals	23	Is_closest_to	857301
Oil_platforms	2	Is_in	171441
Oil_gas_refineries	16	Is_polarized_by	35
Harbors	320	was_obtained_in	35
Dark_spots	171731		
Countries	9		
Basin	7		

image, as shown in Fig. 8. As can be seen, we linked multi-source data together through a reasonable organization that no longer exists in isolation. There are rich semantic relationships between them. To make application and management easier, we must select an appropriate method to store it. Typically, there are two ways to store knowledge graphs: (1) a RDF (Wylot et al., 2018) format storage and (2) a graph database. RDF format stores data in the form of triples (subject, predicate, object). While this method is simple and easy to implement, the search efficiency of triples is relatively low. Compared to RDF format storage, graph databases are more straightforward. At present, the most typical open-source database is Neo4j (Hao et al., 2021). Neo4j has a complete graph query language and supports most graph mining algorithms, such as PageRank, Label Propagation, and Minimum Weight Spanning Tree. As a result, we chose the Neo4j graph database to store our constructed knowledge graph. However, due to the incompleteness of data in some cases, a knowledge graph has the phenomenon of missing knowledge. Therefore, knowledge reasoning is necessary for discovering implicit knowledge and perfecting it. Previous research in the literature has classified such reasoning methods into three categories (Chen et al., 2020): (1) rule-based reasoning, (2) neural network-based reasoning, and (3) distributed representation-based reasoning. Although rule-based reasoning can simulate human reasoning, the reasoning rules are difficult to define (Chen et al., 2020). Neural network-based reasoning exhibits strong reasoning ability but poor interpretability (Ji et al., 2021). Distributed representation-based reasoning can make the best of structural information in a knowledge graph, but it lacks the consideration of deeper information (Chen et al., 2020). Generally, these three approaches are complementary and can be used jointly in inference tasks.

Our main reasoning task was to discriminate oil spill entities (i.e., entity classification). The following problems eventually were encountered (Topouzelis, 2008): missing oil spill data and unbalanced labels in the dataset (the number of oil spill dark spots was small, and the non-oil patches accounted for the vast majority of the dark spots). We decided

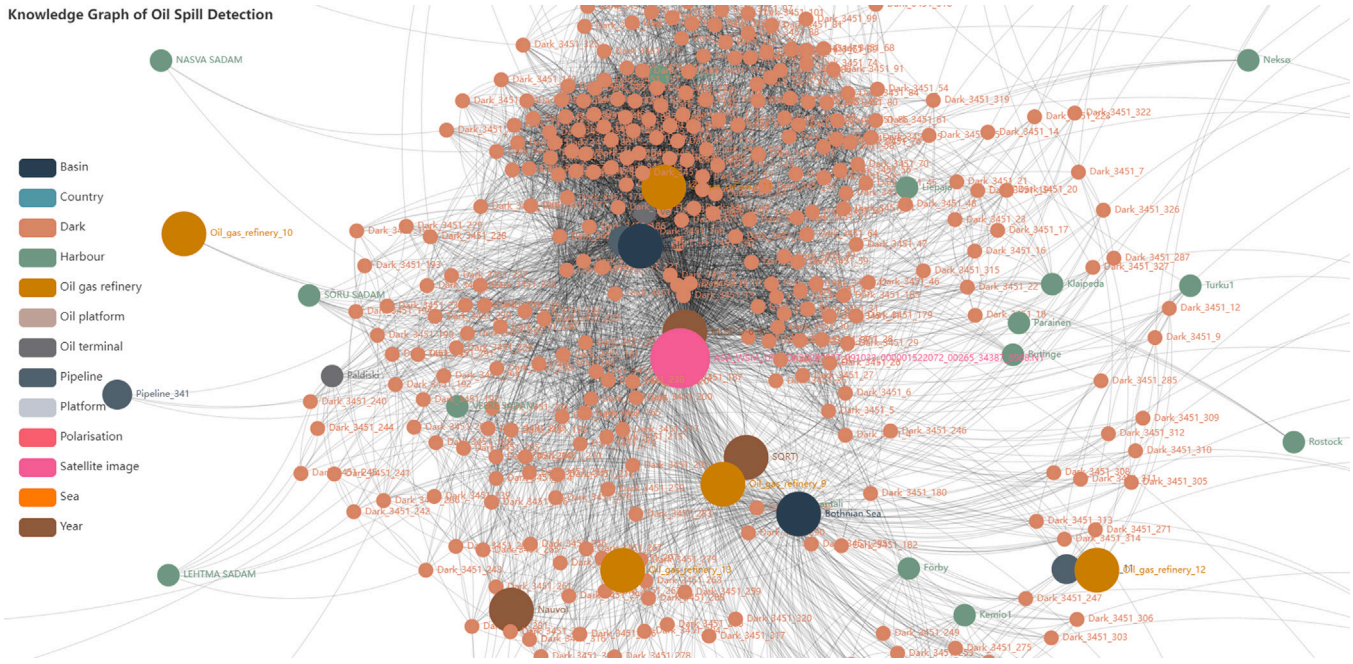

Fig. 8. Visualization of parts of nodes and relations in oil spill detection knowledge graph.

to use an oil spill reasoning method based on our knowledge graph, which combined rule inference and GNN algorithms. This method was expected to alleviate the impact of label imbalance in the dataset and consisted of three steps: (1) distinguishing obvious lookalikes based on features, (2) inference of lookalikes based on the distances between entities, and (3) classification of the remaining dark spots. The first two steps were rule inference, and the third step was graph neural network inference. The specifics were detailed in Algorithm 1 and in the following subsections.

Algorithm 1. Oil spill reasoning method based on the knowledge graph.

Input: The constructed oil spill detection knowledge graph;
Output: Class of dark spots entities;

1: Set feature thresholds and a distance threshold $\boldsymbol{d_{min}}$ using statistical methods;
2: Set an empty collection $\boldsymbol{A}$, rely on feature thresholds to identify parts of lookalikes in advance from dark spot entities, and add them to set $\boldsymbol{A}$ (step 1);
3: Set $\boldsymbol{t = 1}$, and set $\boldsymbol{B}$ as the collection of oil spill candidate entities to be identified;
4: **while** $\boldsymbol{t \neq 0}$ **do**
5: $\boldsymbol{t = 0}$
6: **for all** $\boldsymbol{a}$ in $\boldsymbol{A}$ **do**
7: **for all** $\boldsymbol{b}$ in $\boldsymbol{B}$ **do**
8: **if** distance between $\boldsymbol{b}$ and $\boldsymbol{a} < \boldsymbol{d_{min}}$ **then**
9: Take $\boldsymbol{b}$ out of $\boldsymbol{B}$ and add it to $\boldsymbol{A}$, $\boldsymbol{t = t + 1}$
10: **end if**
11: **end for**
12: **end for**
13: **end while**
14: Utilize graph neural network technology to classify oil spill candidate entities in set $\boldsymbol{B}$ (step 3)

3.3.1. Rule-based reasoning

Generally, some lookalikes display distinct differences in some characteristics compared to oil slicks. For example, too large or too small dark spots are not oil slicks. Likewise, dark spots on the sea surface where winds exceeding a certain range are unlikely to be oil slicks, as are dark areas away from the source of the oil spill. Relying on these differences, we made a preliminary classification of dark spots by setting simple feature thresholds. According to the statistics of 4000 oil slicks detected from SAR images between 1992 and 2015, Najoui et al. (2017) found that 95% of the oil slicks could be detected when the wind speed ranged from 2.09 m/s to 8.33 m/s, but they could not be detected when the sea wind speed was too high or too low. Therefore, they inferred that those dark spots with high or low wind speed were lookalikes. Other authors have conducted similar work; for example, Mera et al. (2017) eliminated the dark spots caused by low wind speeds from their dataset before oil spill detection, which reduced the number of dark spots that needed to be distinguished. We also made some inferences based on location information. Since oil spills mainly occur in some areas close to leak sources, such as ship tracks, oil terminals, ports, oil pipelines, and oil platforms, we inferred those dark spots in regions away from leak sources as lookalikes. In addition, according to the amount of oil spilled, we inferred those dark spots with excessively large or small areas were not oil slicks. Previous work in the literature also directly removed small areas of dark spots before identifying oil slicks (Taravat et al., 2013).

Table 6, based on the above inferences, shows the division of the dark spots into six categories according to their distance from different leakage sources and six collections ($\boldsymbol{C1}$, $\boldsymbol{C2}$, $\boldsymbol{C3}$, $\boldsymbol{C4}$, $\boldsymbol{C5}$, $\boldsymbol{C6}$) are set to store them. These collections are not likely the whole source of oil spills in the Baltic Sea, but we believe that most of them are covered here. The main sources of oil spills in this sea are known to be ships (Konik and Bradtke, 2016). The thresholds for the first step inference include the maximum oil spill area, the minimum oil spill area, and the maximum distance from the oil spill to the leak source for each category. In addition, we also determined the maximum wind speed threshold $\boldsymbol{w_{max}}$ and the minimum wind speed threshold $\boldsymbol{w_{min}}$ to separate more lookalikes. The inference rules are listed as Eq. (1) through 7 below, which are the first step of our inference algorithm, where ***rule*1** to ***rule*6** are used to infer lookalikes from six different categories of dark spots while ***rule*7** is used to infer lookalikes depending on the wind speed thresholds. In these formulas, $\boldsymbol{i}$, $\boldsymbol{j}$, $\boldsymbol{k}$, $\boldsymbol{l}$, $\boldsymbol{m}$, $\boldsymbol{n}$, and $\boldsymbol{o}$ denote dark spots in different sets and $\boldsymbol{ow}$ is the wind speed

Table 6
Sets and feature thresholds required for rule inference.

Categories	Sets	Maximum distance from oil spill to leak source	Maximum oil spill area	Minimum oil spill area
The dark spots closest to ship trajectories	$i \in C1$	$d1_{max}$	$a1_{max}$	$a1_{min}$
The dark spots closest to oil pipelines	$j \in C2$	$d2_{max}$	$a2_{max}$	$a2_{min}$
The dark spots closest to harbors	$k \in C3$	$d3_{max}$	$a3_{max}$	$a3_{min}$
The dark spots closest to oil terminals	$l \in C4$	$d4_{max}$	$a4_{max}$	$a4_{min}$
The dark spots closest to oil gas refineries	$m \in C5$	$d5_{max}$	$a5_{max}$	$a5_{min}$
The dark spots closest to oil platforms	$n \in C6$	$d6_{max}$	$a6_{max}$	$a6_{min}$

of the dark spot o. i_d, j_d, k_d, l_d, m_d, and n_d represent the distance of the remaining dark spots from their nearest oil spill source, while i_a, j_a, k_a, l_a, m_a, and n_a refer to their areas. Relying on the above rules and thresholds, we pre-identified some obvious lookalike entities and stored them in set A, while unidentifiable entities were saved in set B. All of these feature thresholds need to be determined using statistical methods.

$$rule1 = \neg((i_d < d1_{max}) \wedge (i_a < a1_{max}) \wedge (i_a > a1_{min})), i \in C1 \quad (1)$$

$$rule2 = \neg((j_d < d2_{max}) \wedge (j_a < a2_{max}) \wedge (j_a > a2_{min})), j \in C2 \quad (2)$$

$$rule3 = \neg((k_d < d3_{max}) \wedge (k_a < a3_{max}) \wedge (k_a > a3_{min})), k \in C3 \quad (3)$$

$$rule4 = \neg((l_d < d4_{max}) \wedge (l_a < a4_{max}) \wedge (l_a > a4_{min})), l \in C4 \quad (4)$$

$$rule5 = \neg((m_d < d5_{max}) \wedge (m_a < a5_{max}) \wedge (m_a > a5_{min})), l \in C5 \quad (5)$$

$$rule6 = \neg((n_d < d6_{max}) \wedge (n_a < a6_{max}) \wedge (n_a > a6_{min})), l \in C6 \quad (6)$$

$$rule7 = (o_w < w_{min}) \vee (o_w > w_{max}), o \in C, \quad C = C1 \cup C2 \cup C3 \cup C4 \cup C5 \cup C6 \quad (7)$$

$$rule1 \vee rule2 \vee rule3 \vee rule4 \vee rule5 \vee rule6 \vee rule7 \vee \Rightarrow A \quad (8)$$

Empirically, two close-together dark spots on one image have the same labels, and are thought to be similar to a label propagation algorithm (Wang and Zhang, 2008). According to this rule and relying on the entities in set A, we performed the second step of reasoning to identify more lookalikes. Likewise, we needed to use statistical methods to set the distance threshold d_{min}. Using the knowledge graph, we retrieved the dark spots in set B whose distance to the entities in set A less than the threshold d_{min}, and added them to set A. We performed iterative calculations until the distance between all entities in set B and the entities in set A was greater than d_{min}.

3.3.2. GNN-based reasoning

Since the entities in set A were all inferred to be non-oil patches, we only needed to classify the entities in set B. Firstly, we must lower the dimensionality of the dark spot features to minimize the complexity of the learning job. Similar to the work of Mera et al. (2017), we used the SVM-RFE feature selection algorithm to find the best feature combination for oil spill detection. The F1 score (Aftab et al., 2022), which is the harmonic mean of precision and recall, was used to assess the performance of various feature combinations. This metric considers both precision and recall and has been widely used to assess classification accuracy (Zeid et al., 2021). To fully exploit the entity characteristics in set B as well as the relationship properties between these entities, we reconstructed a graph $G = (V, E)$, where $V = \{v_1, v_2, \ldots, v_i, v_i{+}1, \ldots, v_N\}$ and $E \subseteq V \times V$ were the sets of vertices and edges in set B, respectively. The node v_i represented the graph's ith entity, and the edge $e_{i,j} = (v_i, v_j) \in E$ indicated that the entity v_i was connected to v_j. Following that, the DeeperGCN model (Li et al., 2020), a state-of-the-art graph neural network model, was used for graph node classification. This model employs certain neighborhood aggregation functions to aggregate node features, neighbor node features, and relationship features in graph data into higher-level features layer by layer to improve the performance of graph node classification. The formula (9)–(11) describes the particular aggregation process of each layer (Li et al., 2020),

$$m_{vu}^{(l)} = RELU\left(h_u^{(l)} + 1\left(he_{vu}^{(l)}\right) \cdot he_{vu}^{(l)}\right) + \epsilon, \quad u \in N(v) \quad (9)$$

$$m_v^{(l)} = \zeta^{(l)}\left(\left\{m_{vu}^{(l)} | u \in N(v)\right\}\right) \quad (10)$$

$$h_v^{(l+1)} = MLP\left(h_v^{(l)} + s \cdot \left\|h_v^{(l)}\right\|_2 \cdot m_v^{(l)} / \left\|m_v^{(l)}\right\|_2\right) \quad (11)$$

where $h_v^{(l)}$ and $h_u^{(l)}$ are node features of nodes v and u in layer (l), respectively. The edge features of node v to u in layer (l) are denoted by $he_{vu}^{(l)}$. $N(v)$ represents the set of neighbor nodes of v. $ReLU(.)$ denotes the rectified linear unit (Hara et al., 2015), while $\mathbf{1}(.)$ denotes the indicator function, which is 1 when the edge feature occurs and 0 otherwise. $MLP(.)$ is a multi-layer perceptron (Longstaff and Cross, 1987), ϵ is a tiny constant with a value of 10–7, and s is a learnable scaling factor. $\zeta(l)$ is a differentiable message aggregation function, such as $SoftMax$, $PowerMean$ (Li et al., 2020). All layers are linked together using a variant of residual connections (res+), and finally, a linear layer is used to output the model classification results. The cross entropy loss function L (Zhu et al., 2021) is chosen as the model optimization function, and all the above learnable parameters can be updated by the back-propagation algorithm.

$$L = -1/N \sum_{i=1}^{N} \left(y_i \log p_i + \left(1 - y_i\right)\left(1 - \log p_i\right)\right) \quad (12)$$

where y_i is the ground-truth label and $y_i \in (0, 1)$, while p_i is the predicted probability of being an oil spill object i. N is the number of dark spots. Compared with existing oil spill detection methods, this graph neural network technology can more effectively combine other information other than dark spot features to help detect oil slicks.

3.4. Experiment settings

This subsection describes the specific experimental setup for oil spill detection inference, including dataset splitting, evaluation metrics, and implementation details.

3.4.1. Dataset splitting

To make it easier to compare oil spill detection algorithms, we split our dataset into three categories. Among the 35 SAR images, 18 were randomly selected as the training set, 7 as the test set, and 10 as the validation set. There were 110 oil slicks discovered in the training set, 36 in the test set, and 35 in the validation set. The ratio of detected oil slick patches was about 6:2:2. Table 7 lists the statistics of lookalikes and oil slicks in the different sets. The ratio of oil spill pixels to lookalike pixels was about 6:10,000, and the number of lookalikes in each set considerably outnumbered the number of oil spills. We called the dataset consisting of all 35 SAR images the "initial dataset". Unless otherwise noted, all oil spill detection experiments in the following sections were based on this dataset.

Table 7
Ground truth in the training set, validation set, and test set.

Category	Number of images	Number of oil slick	Number of lookalikes	Number of oil slick pixels	Number of lookalike pixels
Training set	18	110	66264	116291	91504249
Validation set	10	35	69005	10666	102662699
Test set	7	36	36281	28416	40996854

3.4.2. Evaluation measures

To assess the effectiveness of oil spill detection, we chose three pixel-level metrics: *Sensitivity* (Seydi et al., 2021), *Specificity* (Yekeen et al., 2020), and *Precision* (Mera et al., 2017), which are frequently used in oil spill detection algorithm evaluations. *Sensitivity* denotes the algorithm's ability to correctly identify oil spills, *Specificity* refers to the algorithm's ability to accurately identify lookalikes, and *Precision* refers to the eventual oil spill detection accuracy. These metrics are defined as follows (Mera et al., 2017):

$$Sensitivity = TP/(TP + FN) \tag{13}$$

$$Specificity = TN/(TN + FP) \tag{14}$$

$$Precision = TP/(TP + FP) \tag{15}$$

In the above equations, TN (True Negatives) and TP (True Positives) represent the number of pixels with correctly identified lookalikes and oil spills, respectively. FP denotes False Positives (the number of pixels at which lookalikes are identified as oil spills) and FN represents False Negatives (the number of pixels at which oil spills are identified as lookalikes).

3.4.3. Implementation details

We used the Adam optimizer with an initial learning rate of 0.0001 to implement the DeeperGCN model based on PyTorch Geometric. The batch size was 1, the hidden channel size was 384, and the dropout was 0.1. The number of GCN layers was 3. The message aggregation function was $softmax\_sum$.

4. Results

In this section, we first describe the results of rule inference based on the knowledge graph, then the results of graph neural network inference based on the knowledge graph, and deep mining of oil spill information.

4.1. Superiority verification of the rule-based reasoning module

By counting the distances of the 4525 oil spills detected in the Baltic Sea region published by HELCOM from 1998 to 2017 to the nearest spill sources, we determined that 96% of the oil spills were nearest to ship trajectories, 1% were nearest to harbors and oil terminals, and 3% were nearest to oil pipelines. Our statistical results as shown in Fig. 9 a to c, most of the oil spills closest to ship trajectories were within 1100 m, and their largest oil spill area was 240 km^2. All the oil spills nearest to oil pipelines occurred within 900 meters of them, with the largest oil spill area of about 3 km^2. The remaining oil spills were closest to oil terminals and harbors and were within 850 meters from them, with the largest oil spill area of about 4.14 km^2. Since the area published by HELCOM may not be the final area detected on the SAR imagery, it was not accurate to use them as inference thresholds. Typically, evaporation, emulsification, and other processes gradually altered the nature of the oil spill until it eventually reached a stable emulsified state that was several times larger than its original size. For our purposes, we set this value at 3.5 times and multiplied it by the maximum areas published by HELCOM to obtain the maximum area thresholds for different categories, as shown in Table 8. We tested these area thresholds using 181 oil patches segmented from 35 SAR images between 2006 and 2011; and as shown in Fig. 9, all of the oil patches were within the thresholds. In addition, we set the minimum area threshold at six pixels to filter out small areas of dark spots. Panel f in Fig. 9 showed the frequency distribution of the wind speeds in the 181 oil slick regions. As can be seen, the wind speeds were between 0.98 m/s and 11.2 m/s so we set the w_{min} and w_{max} values to 0.98 m/s and 11.2 m/s, respectively.

Likewise, distance threshold d_{min} was obtained by statistical methods. As shown in Fig. 10, we tested different thresholds ranging from 500 to 2000 at intervals of 50. When the distance threshold exceeded 1100 m, we found that oil spills were added to set A, so we set its value to 1100 m. Relying on the feature thresholds, 55,274 lookalike patches were first separated and added to set A. Then, using distance threshold d_{min}, an additional 78,186 lookalikes were identified and added to set A. Through this pre-recognition, 133,460 lookalikes were filtered out, and the remaining 38,271 oil slick candidates required further identification by GNN-based reasoning.

4.2. Feature selection and GNN-based inference

Following attribute extraction, each oil spill candidate got a vector with 234 feature values related to the feature space specified in Section 3.2.2 (including 52 features reported by Mera et al., 2017 and 13 new features presented in this study). To reduce the learning complexity, the SVM-RFE method was employed to find the best combination to distinguish the remaining dark spots. It works by training an SVM classifier iteratively, ranking the scores of each feature value based on the SVM weights, removing the feature value with the lowest score, and finally selecting the feature values required. The 13 features we proposed are ranked as follows: DAIS, Rm, DT, Cam, Sm, Sp, DOGR, DOP, DH, DP, DC, Tm, and AISdm. Fig. 11 depicts the F1 score change of the SVM algorithm after sequentially adding them to the previous 52 features. The F1 score was zero when using only 52 features, which was due to the extreme label imbalance in our dataset. When DAIS was incorporated, the F1 score increased to 9.3%. Following that, adding the four features of Rm, DT, Cam, and Rm in turn, the F1 score increased to 13.3%. We continued to add Sp and DOGR, and the corresponding F1 score rose again to 21.28%. When we added the remaining features in sequence, the corresponding F1 score did not change significantly. Obviously, the top seven features among the 13 we proposed were the most beneficial for oil spill detection. After that, we assessed the performance of various feature combinations and eventually determined that 114 feature values had the highest F1 score. These corresponding features were taken as the optimal feature subset, as shown in the supplementary material.

Table 9 shows the quantitative results of graph neural network inference with various feature inputs, including the 52 features reported by Mera et al. (2017), all 65 features (52 features utilized by Mera et al., 2017, and 13 features presented in this study), and the optimal subset of features proposed. We discovered that when employing the 52 features, 11 out of 36 oil spills were accurately inferred, whereas 7 lookalikes were mistakenly classified as oil spills. However, after adding 13 new features we proposed, 17 oil spills were successfully detected, whereas 13 lookalikes were misidentified. Furthermore, 21 oil spills were correctly identified and 16 lookalikes were misclassified when using optimal feature subset we suggested for reasoning. Obviously, using the optimal subset of features for oil spill inference was obviously the best choice, followed by the 65 and 52 features. 13 new features we proposed considerably increase the capacity to detect oil spills.

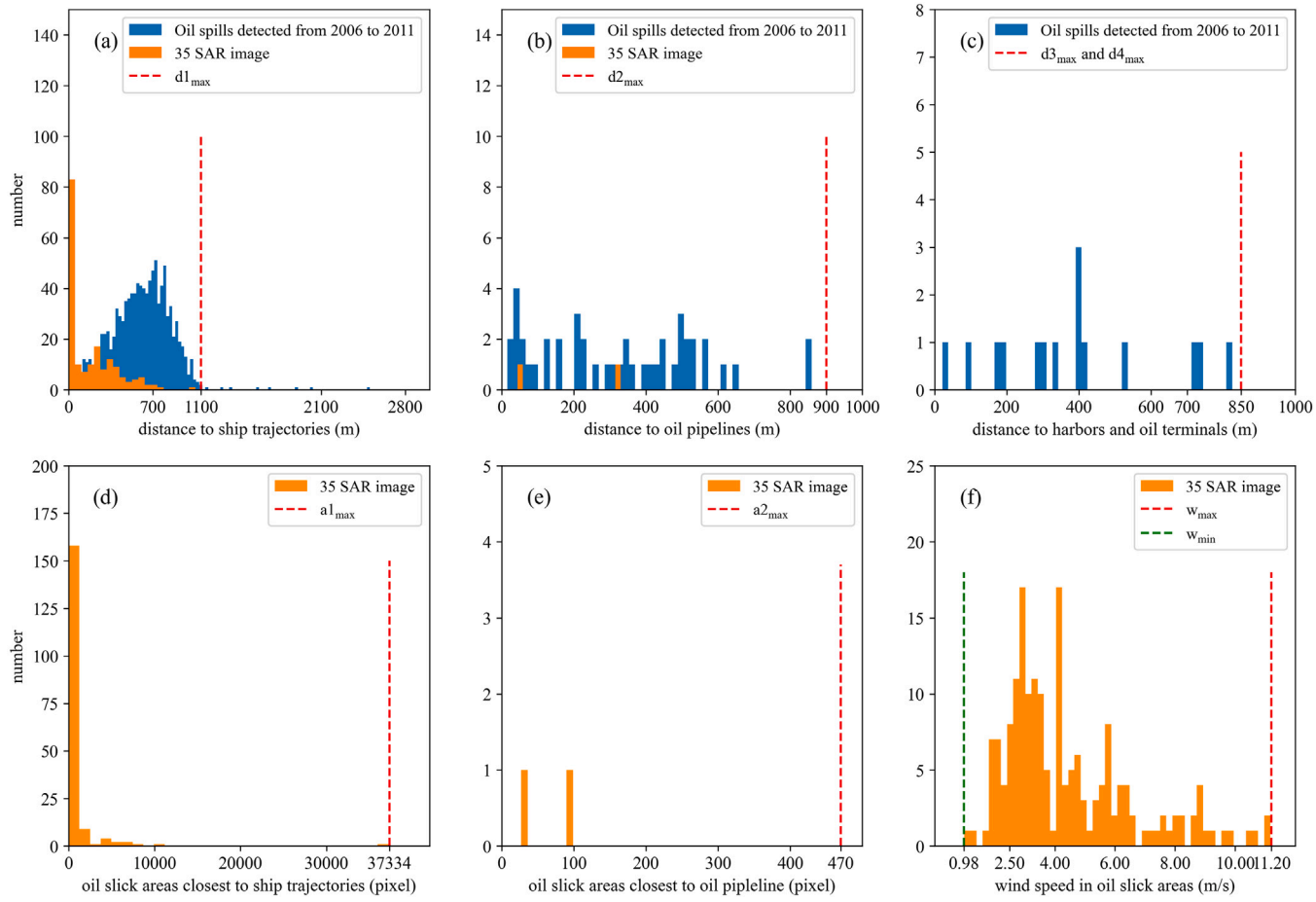

Fig. 9. Determination and verification of feature thresholds. Panels a to c show the frequency distribution of the distance from oil slicks to the nearest ship tracks, the frequency distribution of the distance from oil slicks to the nearest oil pipelines, and the frequency distribution of the distance from oil slicks to the nearest harbors or oil terminals, respectively. Panels d and e show the frequency distribution of the area of oil slicks closest to different oil spill sources. Panel f shows the frequency distribution of the wind speeds for 181 oil slick regions segmented from 35 SAR images.

Table 8
Features thresholds for segregating some lookalikes.

Name	Value	Name	Value (m)	Name	Value (pixel)	Name	Value (pixel)
$C1$	$C1 \neq \varnothing$	$d1_{max}$	1100	$a1_{max}$	37334	$a1_{min}$	6
$C2$	$C2 \neq \varnothing$	$d2_{max}$	900	$a2_{max}$	470	$a2_{min}$	6
$C3$	$C3 \neq \varnothing$	$d3_{max}$	850	$a3_{max}$	644	$a3_{min}$	6
$C4$	$C4 \neq \varnothing$	$d4_{max}$	850	$a4_{max}$	644	$a4_{min}$	6
$C5$	$C5 = \varnothing$	$d5_{max}$	–	$a5_{max}$	–	$a5_{min}$	–
$C6$	$C6 = \varnothing$	$d6_{max}$	–	$a6_{max}$	–	$a6_{min}$	–

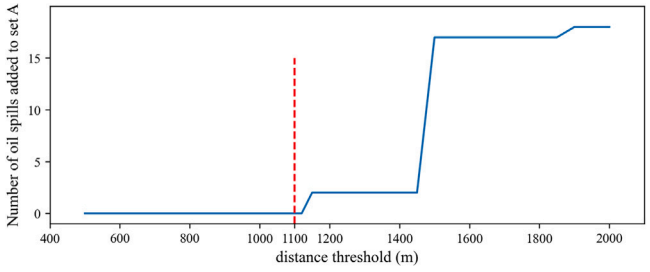

Fig. 10. The effect of different distance thresholds on dark spots recognition.

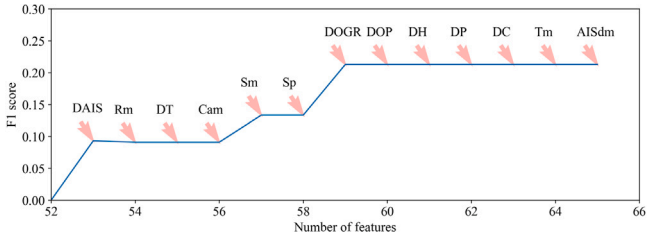

Fig. 11. Importance measure of our proposed 13 new features.

Additionally, the optimal feature subset can further improve oil spill detection performance with fewer input characteristics. All subsequent graph neural network inferences took the optimal feature subset as input.

4.3. Deep information mining of detected oil spills

A large number of oil spill patches are effectively identified through knowledge reasoning. To make our knowledge graph complete and use it to mine some hidden information related to these oil spill patches,

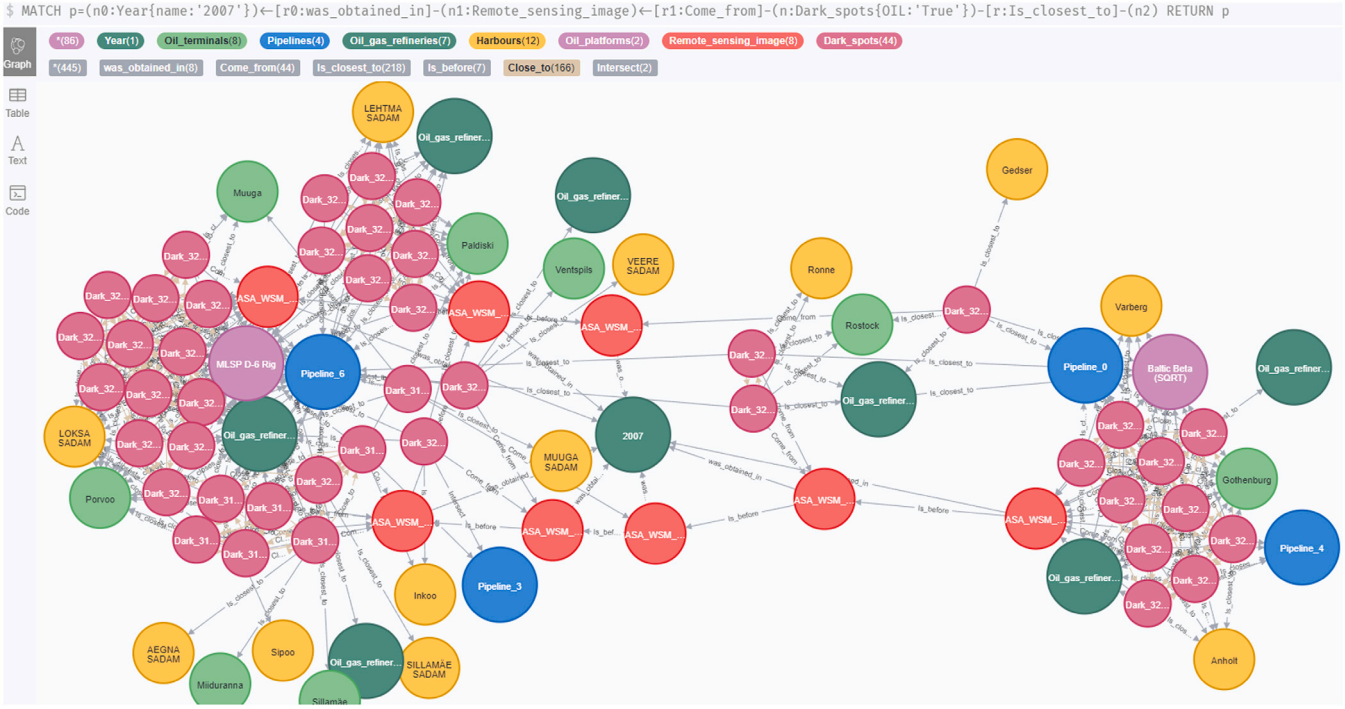

Fig. 12. Harbors, pipelines, oil and gas refineries, oil terminals, and oil platforms closest to the oil spill patches detected from different images in 2007.

Table 9
Quantitative results of oil spill detection based on knowledge graph.

Methods	*Sensitivity*	*Specificity*	*Precision*
Knowledge Graph Reasoning with 52 features	0.6760	0.9984	0.2259
Knowledge Graph Reasoning with 65 features	0.8293	0.9981	0.2358
Knowledge Graph Reasoning with the optimal feature subset	**0.8428**	**0.9985**	**0.2781**

Table 10
The distance between oil spill patches, nearest oil terminals and harbors, etc. and countries to which this oil terminals, harbors, and oil platforms belong.

Oil spill patches	Distance (m)	Terminals	Harbors	Oil platforms	Countries
Dark_3220_298	48824.551	Rostock	–	–	Germany
Dark_3220_298	18546.653	–	Gedser	–	Denmark
Dark_3220_298	431019.108	–	–	Baltic Beta (SQRT)	Poland
Dark_3105_2247	578274.250	–	–	MLSP D-6 Rig	Russia
Dark_3105_2247	48420.794	Porvoo	–	–	Finland

all reasoning results must be integrated into the knowledge graph by knowledge completion. In this study, we constructed two new entities with the label "types of dark spots" in the knowledge graph, named "oil slicks" and "lookalikes", respectively. If dark spots were inferred to be lookalikes, created a *is classified as* relationship between them and the lookalikes entity; otherwise, added a *is classified as* relationship between them and the oil slicks entity. Because inference errors are inevitable, the knowledge graph must also be corrected after the on-site inspection and verification. Furthermore, we inferred that the dark spots with speeds less than $\boldsymbol{w}_{min}$ were caused by the slow wind speed, and we added these inferences to the knowledge graph by constructing new entities with the low wind speed label while establishing *cause* relationships between the low wind speed entities and the dark spot entities. For other causes of dark spots, we could not infer due to the lack of labeled data, thus leaving them to future work.

The completed knowledge graph can provide numerous users with convenient oil spill knowledge query and knowledge service capabilities. Fig. 12, Tables 10, and 11 show several knowledge retrieval examples, respectively. Fig. 12 shows the search for oil spill patches detected from different images in 2007 and our query of their nearest harbors, pipelines, oil and gas refineries, oil terminals, and oil platforms that may be sources of oil spills. Table 10 indicates the distances of each oil spill patch to the nearest harbors, oil platforms, oil terminals, etc., and retrieves the countries to which these ports, oil platforms, and oil terminals belong. If the distance was very close, the corresponding pipelines, oil platforms, and oil and gas refineries needed to be further inspected for damage or oil discharge. Based on these query results, it also was possible to contact the corresponding country and then dispatch ships from closer ports for clean-up. Table 11 shows the number of oil spill patches found in each sea basin in a given year. It can reflect the degree of threat of oil spills in different areas, which

Table 11
Number of oil spill patches in various sea basins in 2007.

Sea basins	Count	Sea basins	Count
Danish Straits	1	Gulf of Finland	22
Baltic Proper	11	Kattegat	10

Table 12
Comparison of our method with several excellent oil spill detection methods on different datasets. The pixel ratio of oil spills to lookalikes in the initial dataset is 6:10000, while it is 1:5.5 in the new dataset.

Methods	Initial dataset			New dataset		
	Sensitivity	*Specificity*	*Precision*	*Sensitivity*	*Specificity*	*Precision*
SVM with 6 features (Mera et al., 2017)	0	**1**	–	0.5781	**0.99997**	**0.9758**
UNet (Krestenitis et al., 2019)	0	**1**	–	0.7415	0.84654	0.3925
DeepLabv3+ (Krestenitis et al., 2019)	0	**1**	–	0.6025	0.94800	0.5791
MCAN (Li et al., 2021b)	0	**1**	–	0.0131	0.99982	0.2781
SDGCN (Liu et al., 2022)	0	**1**	–	0.2052	0.97572	0.4826
Our Knowledge Graph Reasoning	**0.8428**	0.9985	**0.2781**	**0.9114**	0.99991	0.9607

is beneficial to managers for developing different strategies to monitor and manage various sea areas. More knowledge queries are available in the supplementary material.

5. Discussion

In this Section, we discuss the performance of our knowledge graph-based oil spill detection techniques against existing methods, as well as the benefits and future work of the knowledge graph for oil spill detection.

5.1. Comparison with the baselines

Five existing representative oil spill dark spot detection methods, including SVM with six selected feature values (Mera et al., 2017), UNet (Krestenitis et al., 2019), DeepLabv3+ (Krestenitis et al., 2019), MCAN (Li et al., 2021b), and SDGCN (Liu et al., 2022), were compared to our knowledge graph-based approach. Although SDGCN was previously used for dark spot segmentation in our knowledge graph, we retrained it on the oil spill dataset and used it to detect oil spill patches in SAR images here.

Table 12 shows the quantitative results of various oil spill detection algorithms. Experiments demonstrated that, although exhibiting good performance on their own datasets, these state-of-the-art baseline approaches failed to recognize any oil slicks in our initial dataset and labeled all samples as lookalikes. The main reason for this problem was the extreme class imbalance in our initial dataset (the ratio of oil spill pixels to lookalike pixels was about 6:10,000), which led to poor performance of other methods. We reviewed their research and discovered that Mera et al. (2017) employed 92 dark spots in their experiment, 47 of which were oil spots and 45 of which were lookalikes, with a pixel ratio of roughly 1:2; Krestenitis et al. (2019) employed a dataset with a pixel ratio of 1:5.5 for oil spill patches to lookalikes; and Li et al. (2021b) used only four images of 256*256 pixels to train their proposed MCAN model, and more than 80% of the dark spots in the images were oil spills. The pixel ratio of oil spill patches to lookalikes appears to be very ideal in previous datasets, but the reality is nowhere near as high as they describe. Typically, non-oil patches outnumber real oil spill patches. The imbalance of sample labels is still an unavoidable problem. Since our method uses a knowledge graph-based rule inference approach, 78% of the lookalikes were identified in advance and eliminated from the dataset, thus attenuating the effect of class imbalance. After graph node classification, 21 of the 36 oil slicks in the test set were correctly identified, whereas 15 were missed and 16 lookalikes were identified as oil spots. More than half of the oil spills were correctly detected. Fig. 13 shows several oil spills detected by our method as well as missed oil spill patches. In terms of detection results, although they are not ideal due to the dataset, our technique can detect oil spills even under such extreme label imbalance conditions.

To further illustrate the differences between the above comparison methods, we performed another assessment on a new dataset of 95 images of 512 × 512 pixels. They were all cropped from the original 35 images, with 56 randomly chosen as the training set, 20 as the test set, and 19 as the validation set. The training set included 110 oil spills and 323 lookalikes; the test set consisted of 97 lookalikes and 36 oil spots; and the validation set contained 35 oil spills and 199 lookalikes. The new dataset's pixel ratio of oil spill patches to lookalikes is approximately 1:5.5, which is consistent with the ratio employed by Krestenitis et al. (2019). It is important to note that this ratio is relatively ideal. Because the majority of the dark spots on SAR images may be false non-oil spots, the pixel ratio of detected oil spills to non-oil patches can rarely reach 1:5.5 or higher.

The quantitative results of various oil spill detection algorithms on the new dataset are still shown in Table 12. In addition, Fig. 14 depicts the visualized results of oil spill patches by these methods. In terms of *Sensitivity*, our knowledge graph reasoning technique significantly outperformed other methods. A total of 30 out of 36 oil spill patches were detected, and eight lookalikes were mistaken for oil spills. In terms of *Specificity* and *Precision*, the SVM with the six feature values proposed by Mera et al. (2017) slightly outperformed the method we proposed, but not significantly. This algorithm only considered differences in dark spot features and ignored the effect of dark spot spatial relationships, so the number of identified oil spills was restricted. Statistics showed that it correctly detected 19 oil spills, while two lookalikes were mislabeled as oil spills. Nonetheless, this method still outperformed the remaining four deep learning-based oil spill detection techniques in terms of Precision metrics. The reason for this is that the excellent SDGCN model (Liu et al., 2022) improves the performance of dark spot segmentation, which leads to an improvement in the quality of feature extraction and, ultimately, improves the accuracy of the SVM algorithm for dark spot classification. However, as shown in Table 12 and Fig. 14, directly training the SDGCN model for oil spill detection does not appear to be ideal. This algorithm was developed for dark spot segmentation on SAR images. It segmented SAR imagery into superpixel patches and classified them based on handcrafted features extracted from them. Superpixel segmentation of SAR images and features extracted from superpixels were not particularly useful in detecting oil spills, according to experimental results. The UNet and DeepLabv3+ models were highly influenced by SAR image speckle noise, making identification of oil spill boundaries challenging. Through further comparison, we found that the UNet model had a larger *Sensitivity* value and DeepLabv3+ had a higher *Precision* metric, indicating that UNet performs better in oil spill identification and DeepLabv3+ performed better overall, which was consistent with the findings of Krestenitis et al. (2019). Furthermore, on this new dataset, the MCAN model continued to underperform. In previous work, Li et al. (2021b) did not assess this model's performance on the labeled unbalanced dataset. This model appeared to be more suited for determining the outlines of oil spills by removing small dark spots surrounding oil spill areas rather than recognizing oil slicks in datasets with unbalanced labels.

Table 13 quantifies the time consumption of different methods on a representative SAR image with a size of 12119 × 7117 pixels, including 904 dark spots. We can see that UNet, DeepLabv3+, and MCAN took significantly less time than other methods, with UNet taking the shortest time. The reason is that they can identify oil spills directly from images without too many processing steps. The remaining three methods required more steps and extracted more manually designed features, resulting in longer processing time. Since our method needed to construct knowledge graph first, it took the longest. The SDGCN algorithm also spent a long time, because it must convert the image into

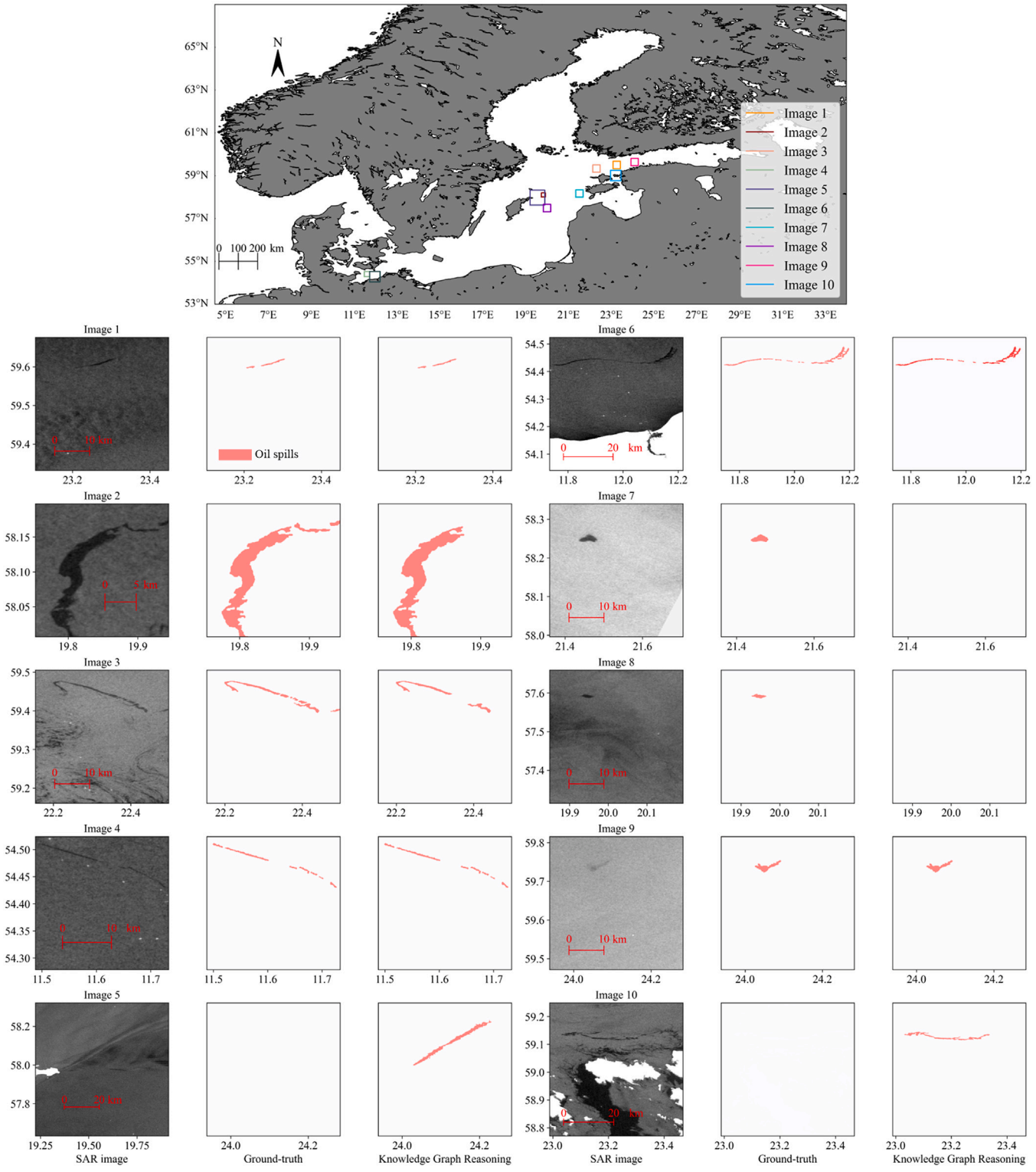

Fig. 13. Oil spill detection results based on knowledge graph. The top panel shows the location of all images. The red patches in the other panels indicate oil spills. (For interpretation of the references to color in this figure legend, the reader is referred to the web version of this article.)

a graph structure with superpixels as nodes before classifying the graph nodes. The BASS algorithm with the higher performance was chosen to complete this step. Even though this algorithm supported GPU acceleration, it still took a long time to complete the superpixel segmentation of a SAR image with 12119 × 7117 pixels. The segmented image was transformed into graphs with 321878 superpixel nodes. Then, for each superpixel, a vector with 137 feature values was extracted, which also increased the processing time. Since both dark spot segmentation and entity extraction used the SDGCN algorithm, these two processes also became time-consuming. Furthermore, attribute extraction and

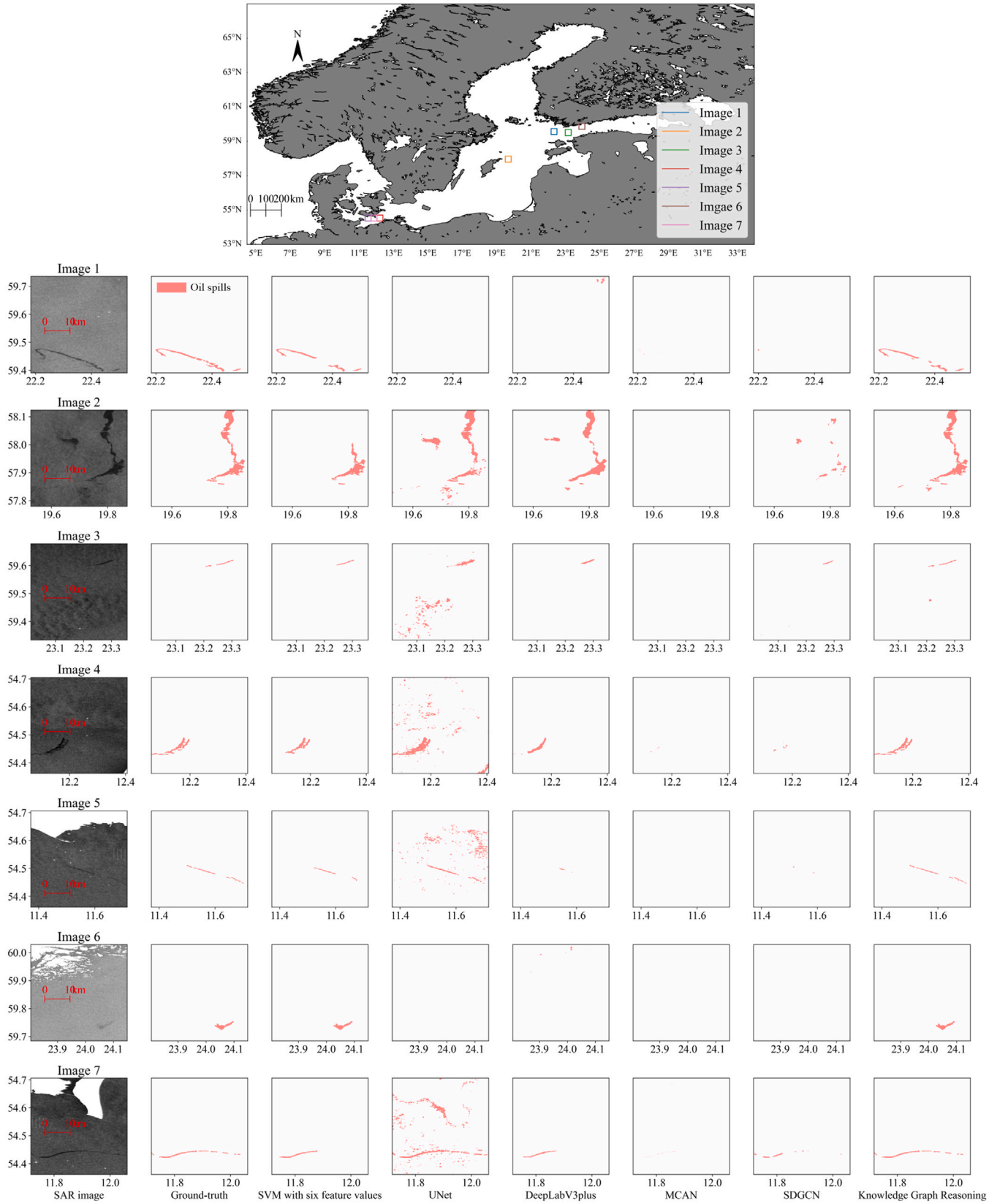

Fig. 14. Oil spill detection results on the new dataset. The top panel shows the location of all images. The red patches in the other panels indicate oil spills. (For interpretation of the references to color in this figure legend, the reader is referred to the web version of this article.)

Table 13
Time-consuming of different models to complete oil spill detection.

Method		Time
Our Knowledge Graph Reasoning	Entity extraction	6.8 h
	Attribute extraction	5.2 h
	Relation extraction	7.7 h
	Rule reasoning	0.9 s
	GNN-based reasoning	2.5 s
SVM with six feature values (Mera et al., 2017)	Dark spot segmentation (Liu et al., 2022)	6.8 h
	Feature extraction	14.2 s
	Dark spot classification	0.02 s
UNet (Krestenitis et al., 2019)		20.4 s
DeepLabv3+ (Krestenitis et al., 2019)		26.7 s
MCAN (Li et al., 2021b)		43.4 s
SDGCN (Liu et al., 2022)	BASS (Uziel et al., 2019)	5.7 h
	Superpixel feature extraction	5.0 h
	Superpixel relation extraction	1.5 min
	Graph node classification	20.7 s

relation extraction also consumed a lot of time because there were a large number of entity attributes and relationships between entities to be extracted to complete the construction of our knowledge graph. However, the reasoning of oil spill identification based on knowledge graphs did not take too much time.

5.2. The superiority of constructing a knowledge graph to detect oil spills

Although SAR satellites are considered an effective tool to detect oil slicks, some satellite sensor factors, such as radar band Najoui et al. (2018), polarization (Najoui et al., 2017), and incident angle (Espedal, 1999), can affect oil spill imaging. Due to the different amounts of oil that may be spilled, the oil slicks reside on the sea surface for different times. These retained oil slicks are subjected to advection (Guo and Wang, 2009), evaporation (Reed et al., 1999), and emulsification (Guo and Wang, 2009) to varying degrees, which can change the characteristics of the oil slicks and may also show image differences. Furthermore, some oceanic and atmospheric phenomena, such as rain cells (Nystuen, 1990), oceanic internal waves (Klemas, 2012), upwelling (Sipelgas and Uiboupin, 2007), low wind speed areas on the sea surface Najoui et al. (2018), and sea currents (Ochadlick Jr. et al., 1992), may show similar characteristics to oil slicks on SAR images. Of all dark spots, more than 99% are likely to be non-oil films rather than oil slicks. The imbalance of labels is a long-standing problem in oil spill detection (Topouzelis, 2008). Although some researchers have demonstrated that deep learning technologies improve the effect of oil spill detection algorithms (Shaban et al., 2021), it is not enough to rely only on deep learning technologies and remote sensing images. First of all, the amount of information obtained only from images is limited, and some valuable information, such as oil pipeline location, ship trajectory, sea temperature difference, and rainfall distribution, may not be considered by the deep learning model. To reduce the memory burden, most models need to take cropped images as input for training, which destroys the shape of dark spots in the image. However, the shape is the most beneficial feature for oil spill identification (Mera et al., 2017). In addition, image cropping also breaks the relationship between dark spots, making them isolated, which is not conducive to oil spills detection. Finally, in practice, the non-oil patches far outnumber the oil slicks in terms of numbers, which often leads to a poor generalization of the trained model and is prone to overfitting. The above situations are why some of the excellent deep learning models in Section 5.1 fail.

The Multi-source knowledge graph for oil spill detection we constructed can accurately describe complex oil spill detection scenes. Some objects, such as oil pipelines, oil terminals, oil and gas refineries, oil platforms, harbors, countries, seas, dark spots segmented from SAR images, satellite platforms, and polarization modes, were extracted and regarded as entities, while rich attributes were extracted for them. Additionally, through semantic computing, the relationships between entities were established so all the information no longer existed in isolation. Our knowledge graph could be stored in the graph database, which provided a solution for the storage of historical oil spill data. Relying on rich entity attributes and semantic relationships would make it easy to query the information that users need as well as uncover some hidden information from the existing entries. Another advantage of our knowledge graph was that it supported efficient reasoning, and the inference results could supplement and improve it. Overall, knowledge graph technology based on multi-source data can be beneficial to the organization and management of new information and knowledge in remote sensing big data. It also can provide convenient remote sensing knowledge query and knowledge service capabilities to many users and can help to comprehensively improve the application capabilities of massive multi-source remote sensing observations.

5.3. Limitations and future work

Since our knowledge graph is aimed at oil spill detection, no additional semantic types, such as the type of oil (Wang et al., 1999), were designed in the model layer. We focused on whether there is an oil leak, no matter what type of oil it is. In addition, some oil spill emergency responses (Krohling and Rigo, 2009), such as the release of oil booms (Cumo et al., 2007), oil slick recovery (Tian et al., 2020), and spraying of anti-oil spill chemical reagents (Niu et al., 2021), are also not considered. We leave them for future work. Since the main data used are remote sensing images, text data occupies only a small part. For convenience, we employed a manual approach to extract knowledge from text data, which is a limitation of the work in this paper. In terms of dark spot features, although we have extracted hundreds of them, it is hard to construct a relatively complete feature set. In the feature subset we proposed, geometric features accounted for the highest proportion, which is consistent with previous studies (Chehresa et al., 2016). Furthermore, we found that the contextual features also occupied a high proportion, indicating that they also played a crucial role in oil spill identification. To improve the performance of oil spill detection, new features that are beneficial to oil spill identification need to be constantly sought in the future. Because it takes a long time to extract knowledge from multi-source data, an accelerated algorithm must also be developed to improve the speed of knowledge extraction in future work. In knowledge reasoning, there is an extreme imbalance between the oil and non-oil labels, which makes it difficult to identify some oil entities. While we used a rule-based reasoning method to eliminate the great majority of non-oil entities in advance, some rule thresholds were set relatively loosely due to the lack of sufficient statistics. According to Fingas (2018), when oil spills onto the sea

surface, it was subjected to evaporation, emulsification, etc., and finally reached a stable emulsion within an area two to five times larger than its original size. In this study, we set this value at 3.5 times. Moreover, we set the w_{min} and w_{max} values to 0.98 m/s and 11.2 m/s, respectively. However, Najoui et al. (2018) found that 95% of the oil slicks could be detected when the wind speed ranged from 2.09 m/s to 8.33 m/s. In future work, more data should be employed to acquire more accurate rules. Furthermore, due to the limited labeled data we used, it was not possible to obtain some other inference rules that could lead to lookalikes phenomena by statistical means, and we therefore will address this limitation in future work as well.

6. Conclusions

In this study, we presented our novel construction of a series of related researches to construct a knowledge graph based on multi-source data to solve the problem of information islands in oil spill detection. Our knowledge graph is the first one specifically designed for oil spill detection in the remote sensing field. Based on expert knowledge, we designed the model layer of the knowledge graph and guided the following knowledge extractions, including entity recognition, attribute extraction, and relation extraction. Then, using multi-source data (vectors, remote sensing images, text, and atmospheric and ocean model data), we extracted valuable knowledge to complete the preliminary building of the knowledge graph. We proposed our knowledge graph to treat a single vector as an independent entity, and its properties can be directly regarded as entity properties, whereby actual objects detected from remote sensing images can be considered entities. This strategy can be used to guide the development of future remote sensing knowledge graphs. We also proposed 13 new dark spot features to help identify oil spills, and experimental results showed that these new features significantly improved oil spill detection performance. After the knowledge graph was constructed, all oil spill-related information was organized together reasonably and no longer existed in isolation. For application convenience, our constructed knowledge graph is stored in the popular Neo4j graph database. Following that, we also proposed a knowledge reasoning method combining rule reasoning and a graph neural network algorithm to differentiate oil slicks from lookalikes. On a dataset with a pixel ratio of oil spills to lookalikes of about 6:10,000, we found that some of the existing oil spill detection methods cannot detect any oil spills, while our technology can identify oil spills under the same conditions with a sensitivity of 0.8428, a specificity of 0.9985, and a precision of 0.2781. Additional experiments revealed that the label imbalance in the dataset was the primary cause of the contrastive methods failing, as well as the high specificity but low sensitivity and precision in knowledge reasoning. Our technique was proven to alleviate the label imbalance problem. After knowledge inference, all inference results can be integrated into the knowledge graph, allowing the knowledge graph to evolve iteratively. Our knowledge graph currently can be used only for oil spill detection; but our future work will explore remote sensing object segmentation methods for applications such as sea ice and ocean internal waves (Barbat et al., 2021), which then could also be incorporated into our knowledge graph to help identify oil spills. In addition, we also plan to study the construction of oil spill response knowledge graphs.

CRediT authorship contribution statement

Xiaojian Liu: Conceptualization, Methodology, Software, Validation, Formal analysis, Investigation, Resources, Data curation, Writing – original draft, Visualization. **Yongjun Zhang:** Writing – review & editing, Supervision, Project administration, Funding acquisition. **Huimin Zou:** Writing – review & editing, Visualization. **Fei Wang:** Writing – review & editing. **Xin Cheng:** Writing – review & editing. **Wenpin Wu:** Writing – review & editing. **Xinyi Liu:** Supervision, Project administration, Funding acquisition. **Yansheng Li:** Writing – review & editing, Supervision, Project administration, Funding acquisition.

Declaration of competing interest

The authors declare that they have no known competing financial interests or personal relationships that could have appeared to influence the work reported in this paper.

Data availability

Data will be made available on request.

Acknowledgments

This work was supported by the National Natural Science Foundation of China under Grant 42030102, 42192581 and 41971284; the Special Fund of Hubei Luojia Laboratory, China under Grant 220100032. The authors would like to thank Guohao Li and David Mera for their coding assistance, as well as the ESA, the European Centre for Medium-Range Weather Forecasts, and the Baltic Marine Environment Protection Commission for their data support.

Appendix A. Supplementary data

Supplementary material related to this article can be found online at https://doi.org/10.1016/j.jag.2022.103153.

References

Aftab, M., Amin, R., Koundal, D., Aldabbas, H., Alouffi, B., Iqbal, Z., 2022. Classification of COVID-19 and influenza patients using deep learning. Contrast Media Mol. Imaging 2022, 8549707. http://dx.doi.org/10.1155/2022/8549707.

Alpers, W., Holt, B., Zeng, K., 2017. Oil spill detection by imaging radars: Challenges and pitfalls. Remote Sens. Environ. 201, 133–147. http://dx.doi.org/10.1016/j.rse.2017.09.002.

Barbat, M.M., Rackow, T., Wesche, C., Hellmer, H.H., Mata, M.M., 2021. Automated iceberg tracking with a machine learning approach applied to SAR imagery: A Weddell sea case study. ISPRS J. Photogramm. Remote Sens. 172, 189–206. http://dx.doi.org/10.1016/j.isprsjprs.2020.12.006.

Chehresa, S., Amirkhani, A., Rezairad, G.-A., Mosavi, M.R., 2016. Optimum features selection for oil spill detection in SAR image. J. Indian Soc. Remote Sens. 44 (5), 775–787. http://dx.doi.org/10.1007/s12524-016-0553-x.

Chen, X., Jia, S., Xiang, Y., 2020. A review: Knowledge reasoning over knowledge graph. Expert Syst. Appl. 141, 112948. http://dx.doi.org/10.1016/j.eswa.2019.112948.

Cumo, F., Gugliermetti, F., Guidi, G., 2007. Best available techniques for oil spill containment and clean-up in the Mediterranean sea. WIT Trans. Ecol. Environ. 103, 9. http://dx.doi.org/10.1007/s11356-015-5543-y.

Espedal, H.A., 1999. Satellite SAR oil spill detection using wind history information. Int. J. Remote Sens. 20 (1), 49–65. http://dx.doi.org/10.1080/014311699213596.

Fan, Y., Rui, X., Zhang, G., Yu, T., Xu, X., Poslad, S., 2021. Feature merged network for oil spill detection using SAR images. Remote Sens. 13 (16), 3174. http://dx.doi.org/10.3390/rs13163174.

Fingas, M., 2018. The challenges of remotely measuring oil slick thickness. Remote Sens. 10 (2), 319. http://dx.doi.org/10.3390/rs10020319.

Ge, Y., Zhang, X., Atkinson, P.M., Stein, A., Li, L., 2022. Geoscience-aware deep learning: A new paradigm for remote sensing. Sci. Remote Sens. 5, 100047. http://dx.doi.org/10.1016/j.srs.2022.100047.

Genovez, P., Ebecken, N., Freitas, C., Bentz, C., Freitas, R., 2017. Intelligent hybrid system for dark spot detection using SAR data. Expert Syst. Appl. 81, 384–397. http://dx.doi.org/10.1016/j.eswa.2017.03.037.

Guo, W.J., Wang, Y.X., 2009. A numerical oil spill model based on a hybrid method. Mar. Pollut. Bull. 58 (5), 726–734. http://dx.doi.org/10.1016/j.marpolbul.2008.12.015.

Guo, H., Wei, G., An, J., 2018. Dark spot detection in SAR images of oil spill using segnet. Appl. Sci. 8 (12), 2670. http://dx.doi.org/10.3390/app8122670.

Guo, Y., Zhang, H.Z., 2014. Oil spill detection using synthetic aperture radar images and feature selection in shape space. Int. J. Appl. Earth Obs. Geoinf. 30, 146–157. http://dx.doi.org/10.1016/j.jag.2014.01.011.

Hao, X., Ji, Z., Li, X., Yin, L., Liu, L., Sun, M., Liu, Q., Yang, R., 2021. Construction and application of a knowledge graph. Remote Sens. 13 (13), 2511. http://dx.doi.org/10.3390/rs13132511.

Hara, K., Saito, D., Shouno, H., 2015. Analysis of function of rectified linear unit used in deep learning. In: 2015 International Joint Conference on Neural Networks. IJCNN, IEEE, pp. 1–8. http://dx.doi.org/10.1109/IJCNN.2015.7280578.

Hersbach, H., Stoffelen, A.D., de Haan, S., 2007. An improved C-band scatterometer ocean geophysical model function: CMOD5. J. Geophys. Res.: Oceans 112 (C3), http://dx.doi.org/10.1029/2006JC003743.

Ji, S., Pan, S., Cambria, E., Marttinen, P., Philip, S.Y., 2021. A survey on knowledge graphs: Representation, acquisition, and applications. IEEE Trans. Neural Netw. Learn. Syst. 33 (2), 494–514. http://dx.doi.org/10.1109/TNNLS.2021.3070843.

Keramitsoglou, I., Cartalis, C., Kiranoudis, C.T., 2006. Automatic identification of oil spills on satellite images. Environ. Model. Softw. 21 (5), 640–652. http://dx.doi.org/10.1016/j.envsoft.2004.11.010.

Kirkland, E.J., 2010. Bilinear interpolation. In: Advanced Computing in Electron Microscopy. Springer, pp. 261–263. http://dx.doi.org/10.1007/978-1-4419-6533-2_12.

Klemas, V., 2012. Remote sensing of ocean internal waves: An overview. J. Coast. Res. 28 (3), 540–546. http://dx.doi.org/10.2112/JCOASTRES-D-11-00156.1.

Konik, M., Bradtke, K., 2016. Object-oriented approach to oil spill detection using ENVISAT ASAR images. ISPRS J. Photogramm. Remote Sens. 118, 37–52. http://dx.doi.org/10.1016/j.isprsjprs.2016.04.006.

Krestenitis, M., Orfanidis, G., Ioannidis, K., Avgerinakis, K., Vrochidis, S., Kompatsiaris, I., 2019. Oil spill identification from satellite images using deep neural networks. Remote Sens. 11 (15), 1762. http://dx.doi.org/10.3390/rs11151762.

Krohling, R.A., Rigo, D., 2009. Fuzzy group decision making for management of oil spill responses. In: Applications of Soft Computing. Springer, pp. 3–12. http://dx.doi.org/10.1007/978-3-540-89619-7_1.

Li, Y., Kong, D., Zhang, Y., Tan, Y., Chen, L., 2021a. Robust deep alignment network with remote sensing knowledge graph for zero-shot and generalized zero-shot remote sensing image scene classification. ISPRS J. Photogramm. Remote Sens. 179, 145–158. http://dx.doi.org/10.1016/j.isprsjprs.2021.08.001.

Li, Y., Lyu, X., Frery, A.C., Ren, P., 2021b. Oil spill detection with multiscale conditional adversarial networks with small-data training. Remote Sens. 13 (12), 2378. http://dx.doi.org/10.3390/rs13122378.

Li, Y., Ouyang, S., Zhang, Y., 2022. Combining deep learning and ontology reasoning for remote sensing image semantic segmentation. Knowl.-Based Syst. 243, 108469. http://dx.doi.org/10.1016/j.knosys.2022.108469.

Li, G., Xiong, C., Thabet, A., Ghanem, B., 2020. DeeperGCN: All you need to train deeper gcns. http://dx.doi.org/10.48550/arXiv.2006.07739, arXiv preprint arXiv:2006.07739.

Liu, X., Li, Y., Liu, X., Zou, H., 2022. Dark spot detection from SAR images based on superpixel deeper graph convolutional network. Remote Sens. 14 (21), 5618. http://dx.doi.org/10.3390/rs14215618.

Longstaff, I.D., Cross, J.F., 1987. A pattern recognition approach to understanding the multi-layer perception. Pattern Recognit. Lett. 5 (5), 315–319. http://dx.doi.org/10.1016/0167-8655(87)90072-9.

Mansourpour, M., Rajabi, M.A., Blais, J., 2006. Effects and performance of speckle noise reduction filters on active radar and SAR images. In: Proc. Isprs, Vol. 36. (1), p. W41, https://www.researchgate.net/publication/239959635.

Marghany, M., Cracknell, A.P., Hashim, M., 2009. Modification of fractal algorithm for oil spill detection from RADARSAT-1 SAR data. Int. J. Appl. Earth Obs. Geoinf. 11 (2), 96–102. http://dx.doi.org/10.1016/j.jag.2008.09.002.

Mera, D., Bolon-Canedo, V., Cotos, J.M., Alonso-Betanzos, A., 2017. On the use of feature selection to improve the detection of sea oil spills in SAR images. Comput. Geosci. 100, 166–178. http://dx.doi.org/10.1016/j.cageo.2016.12.013.

Misra, A., Balaji, R., 2017. Simple approaches to oil spill detection using sentinel application platform (SNAP)-ocean application tools and texture analysis: A comparative study. J. Indian Soc. Remote Sens. 45 (6), 1065–1075. http://dx.doi.org/10.1007/s12524-016-0658-2.

de Moura, N.V.A., de Carvalho, O.L.F., Gomes, R.A.T., Guimarães, R.F., de Carvalho Júnior, O.A., 2022. Deep-water oil-spill monitoring and recurrence analysis in the Brazilian territory using sentinel-1 time series and deep learning. Int. J. Appl. Earth Obs. Geoinf. 107, 102695. http://dx.doi.org/10.1016/j.jag.2022.102695.

Najoui, Z., Deffontaines, B., Xavier, J.-P., Riazanoff, S., Aurel, G., 2017. Wind speed and instrument modes influence on the detectability of oil slicks using SAR images: A stochastic approach. Remote Sens. Environ..

Najoui, Z., Riazanoff, S., Deffontaines, B., Xavier, J.-P., 2018. A statistical approach to preprocess and enhance c-band SAR images in order to detect automatically marine oil slicks. IEEE Trans. Geosci. Remote Sens. 56 (5), 2554–2564. http://dx.doi.org/10.1109/TGRS.2017.2760516.

Niu, H., Li, J., Wang, X., Luo, F., Qiang, Z., Ren, J., 2021. Solar-assisted, fast, and in situ recovery of crude oil spill by a superhydrophobic and photothermal sponge. ACS Appl. Mater. Interfaces 13 (18), 21175–21185. http://dx.doi.org/10.1021/acsami.1c00452.

Nystuen, J.A., 1990. A note on the attenuation of surface gravity waves by rainfall. J. Geophys. Res.: Oceans 95 (C10), 18353–18355. http://dx.doi.org/10.1029/JC095iC10p18353.

Ochadlick Jr., A.R., Cho, P., Evans-Morgis, J., 1992. Synthetic aperture radar observations of currents colocated with slicks. J. Geophys. Res.: Oceans 97 (C4), 5325–5330. http://dx.doi.org/10.1029/91JC01995.

Reed, M., Johansen, Ø., Brandvik, P.J., Daling, P., Lewis, A., Fiocco, R., Mackay, D., Prentki, R., 1999. Oil spill modeling towards the close of the 20th century: Overview of the state of the art. Spill Sci. Technol. Bull. 5 (1), 3–16. http://dx.doi.org/10.1016/S1353-2561(98)00029-2.

Reichstein, M., Camps-Valls, G., Stevens, B., Jung, M., Denzler, J., Carvalhais, N., et al., 2019. Deep learning and process understanding for data-driven Earth system science. Nature 566 (7743), 195–204. http://dx.doi.org/10.1038/s41586-019-0912-1.

Seydi, S.T., Hasanlou, M., Amani, M., Huang, W., 2021. Oil spill detection based on multiscale multidimensional residual CNN for optical remote sensing imagery. IEEE J. Sel. Top. Appl. Earth Obs. Remote Sens. 14, 10941–10952. http://dx.doi.org/10.1109/JSTARS.2021.3123163.

Shaban, M., Salim, R., Abu Khalifeh, H., Khelifi, A., Shalaby, A., El-Mashad, S., Mahmoud, A., Ghazal, M., El-Baz, A., 2021. A deep-learning framework for the detection of oil spills from SAR data. Sensors 21 (7), 2351. http://dx.doi.org/10.3390/s21072351.

Sipelgas, L., Uiboupin, R., 2007. Elimination of oil spill like structures from radar image using MODIS data. In: 2007 IEEE International Geoscience and Remote Sensing Symposium. IEEE, pp. 429–431. http://dx.doi.org/10.1109/IGARSS.2007.4422822.

Solberg, A.H.S., 2012. Remote sensing of ocean oil-spill pollution. Proc. IEEE 100 (10), 2931–2945. http://dx.doi.org/10.1109/JPROC.2012.2196250.

Solberg, A.S., Storvik, G., Solberg, R., Volden, E., 1999. Automatic detection of oil spills in ERS SAR images. IEEE Trans. Geosci. Remote Sens. 37 (4), 1916–1924. http://dx.doi.org/10.1109/36.774704.

Taravat, A., Latini, D., Del Frate, F., 2013. Fully automatic dark-spot detection from SAR imagery with the combination of nonadaptive weibull multiplicative model and pulse-coupled neural networks. IEEE Trans. Geosci. Remote Sens. 52 (5), 2427–2435. http://dx.doi.org/10.1109/TGRS.2013.2261076.

Tian, F., Zhou, J.-f., Shao, C.-l., Wu, H.-b., Hao, L., 2020. Effective recovery of oil slick using the prepared high hydrophobic and oleophilic Fe_3O_4 magnetorheological fluid. Colloids Surf. A 591, 124531. http://dx.doi.org/10.1016/j.colsurfa.2020.124531.

Topouzelis, K.N., 2008. Oil spill detection by SAR images: Dark formation detection, feature extraction and classification algorithms. Sensors 8 (10), 6642–6659. http://dx.doi.org/10.3390/s8106642.

Topouzelis, K., Karathanassi, V., Pavlakis, P., Rokos, D., 2006. Dark formation detection using recurrent neural networks and SAR data. In: Image and Signal Processing for Remote Sensing XII, Vol. 6365. SPIE, pp. 324–330. http://dx.doi.org/10.1117/12.687852.

Topouzelis, K., Karathanassi, V., Pavlakis, P., Rokos, D., 2007. Detection and discrimination between oil spills and look-alike phenomena through neural networks. ISPRS J. Photogramm. Remote Sens. 62 (4), 264–270. http://dx.doi.org/10.1016/j.isprsjprs.2007.05.003.

Topouzelis, K., Stathakis, D., Karathanassi, V., 2009. Investigation of genetic algorithms contribution to feature selection for oil spill detection. Int. J. Remote Sens. 30 (3), 611–625. http://dx.doi.org/10.1080/01431160802339456.

Uziel, R., Ronen, M., Freifeld, O., 2019. Bayesian adaptive superpixel segmentation. In: Proceedings of the IEEE/CVF International Conference on Computer Vision. pp. 8469–8478. http://dx.doi.org/10.1109/ICCV.2019.00856.

Vyas, K., Shah, P., Patel, U., Zaveri, T., Kumar, R., 2015. Oil spill detection from SAR image data for remote monitoring of marine pollution using light weight imagej implementation. In: 2015 5th Nirma University International Conference on Engineering, NUiCONE. IEEE, pp. 1–6. http://dx.doi.org/10.1109/NUICONE.2015.7449646.

Wang, Z., Fingas, M., Page, D.S., 1999. Oil spill identification. J. Chromatogr. A 843 (1–2), 369–411. http://dx.doi.org/10.1016/S0021-9673(99)00120-X.

Wang, F., Zhang, C., 2008. Label propagation through linear neighborhoods. IEEE Trans. Knowl. Data Eng. 20 (1), 55–67. http://dx.doi.org/10.1109/TKDE.2007.190672.

Wylot, M., Hauswirth, M., Cudré-Mauroux, P., Sakr, S., 2018. RDF data storage and query processing schemes: A survey. ACM Comput. Surv. 51 (4), 1–36. http://dx.doi.org/10.1145/3177850.

Xie, H., Yapa, P.D., Nakata, K., 2007. Modeling emulsification after an oil spill in the sea. J. Mar. Syst. 68 (3–4), 489–506. http://dx.doi.org/10.1016/j.jmarsys.2007.02.016.

Yang, Y., Cao, Z., Zhao, P., Zeng, D.D., Zhang, Q., Luo, Y., 2021. Constructing public health evidence knowledge graph for decision-making support from COVID-19 literature of modelling study. J. Saf. Sci. Resil. 2 (3), 146–156. http://dx.doi.org/10.1016/j.jnlssr.2021.08.002.

Yekeen, S.T., Balogun, A.-L., Yusof, K.B.W., 2020. A novel deep learning instance segmentation model for automated marine oil spill detection. ISPRS J. Photogramm. Remote Sens. 167, 190–200. http://dx.doi.org/10.1016/j.isprsjprs.2020.07.011.

Yu, T., Li, J., Yu, Q., Tian, Y., Shun, X., Xu, L., Zhu, L., Gao, H., 2017. Knowledge graph for TCM health preservation: Design, construction, and applications. Artif. Intell. Med. 77, 48–52. http://dx.doi.org/10.1016/j.artmed.2017.04.001.

Yu, X., Zhang, H., Luo, C., Qi, H., Ren, P., 2018. Oil spill segmentation via adversarial f-divergence learning. IEEE Trans. Geosci. Remote Sens. 56 (9), 4973–4988. http://dx.doi.org/10.1109/TGRS.2018.2803038.

Zeid, M.A.-E., El-Bahnasy, K., Abo-Youssef, S.E., 2021. Multiclass colorectal cancer histology images classification using vision transformers. In: 2021 Tenth International Conference on Intelligent Computing and Information Systems. ICICIS, IEEE, pp. 224–230. http://dx.doi.org/10.1109/ICICIS52592.2021.9694125.

Zheng, X., Wang, B., Zhao, Y., Mao, S., Tang, Y., 2021. A knowledge graph method for hazardous chemical management: Ontology design and entity identification. Neurocomputing 430, 104–111. http://dx.doi.org/10.1016/j.neucom.2020.10.095.

Zhou, Z.X., Li, J., Guo, Z.Z., Li, T., 2017. Trade-offs between carbon, water, soil and food in Guanzhong–Tianshui economic region from remotely sensed data. Int. J. Appl. Earth Obs. Geoinf. 58, 145–156. http://dx.doi.org/10.1016/j.jag.2017.01.003.

Zhu, Q., Zhang, Y., Li, Z., Yan, X., Guan, Q., Zhong, Y., Zhang, L., Li, D., 2021. Oil spill contextual and boundary-supervised detection network based on marine SAR images. IEEE Trans. Geosci. Remote Sens. 60, 1–10. http://dx.doi.org/10.1109/TGRS.2021.3115492.